Department of Physics and Astronomy
University of Heidelberg

Master Thesis in Physics
submitted by

Florian Frauen

born in Elmshorn (Germany)

2023

Trigger and Tracking Studies for Charged-Particles Multiplicity Measurements at $\sqrt{s}$ =13.6 TeV with the ATLAS Detector

This Master Thesis has been carried out by Florian Frauen at the
Kirchhoff Institute for Physics in Heidelberg
under the supervision of
Priv.-Doz. Dr. Monica Dunford

Abstract

Charged particle measurements at proton-proton collisions improve our understanding of the strong interaction in the low-energy non-perturbative region. The Minimum Bias analysis measures the primary charged-particles multiplicity at $\sqrt{s} = 13.6\,\text{TeV}$ using low pile-up data taken with the ATLAS detector in 2022. So far, this multiplicity has only been measured for center-of-mass energies up to 13.0 TeV. The new measurement will be an important input to the tuning of Monte Carlo generators.

This thesis presents trigger and tracking studies that are used by the Minimum Bias analysis to correct for detector effects. The Minimum Bias analysis uses a trigger based on the Minimum Bias Trigger Scintillators (MBTS). Its trigger efficiency is measured and found to be lower than in Run 2 due to two dead modules of the MBTS. By measuring the MBTS firing rate for unpaired bunch crossings, the fraction of beam background events is estimated to be $(0.34 \pm 0.05)\,\%$. A data-driven correction to the track reconstruction efficiency is applied to account for the simplified material description in Monte Carlo simulations.

Kurzfassung

Messungen geladener Teilchen bei Proton-Proton-Kollisionen tragen zum Verständnis der starken Wechselwirkung im niedrigenergetischen, nicht-perturbativem Bereich bei. Die Minimum Bias Analyse misst die primary charged-particles multiplicity bei $\sqrt{s} = 13{,}6\,\text{TeV}$ in Daten mit niedrigem pile-up, die mit dem ATLAS-Detektor im Jahr 2022 aufgenommen wurden. Bisher wurde diese nur für Schwerpunktsenergien bis 13,0 TeV gemessen.

In dieser Arbeit werden Trigger- und Tracking-Studien vorgestellt, die von der Minimum Bias Analyse zur Korrektur von Detektoreffekten verwendet werden. Der verwendete Trigger basiert auf den Minimum Bias Trigger Scintillators (MBTS). Dessen Triggereffizienz wurde gemessen und ist aufgrund zweier toter MBTS-Module geringer als in Run 2. Durch eine Messung der MBTS-Feuerrate in ungepaarten bunch crossings wird der Anteil der Strahlhintergrundereignisse auf $(0{,}34 \pm 0{,}05)\,\%$ abgeschätzt. Eine datengetriebene Korrektur der Trackingeffizienz wird angewendet, um der vereinfachten Materialbeschreibung in Monte Carlo Simulationen Rechnung zu tragen.

Contents

1 Introduction

The study of charged particles in proton-proton collisions contributes to a deeper understanding of the strong force in the low-energy non-perturbative domain. In this regime, cross-sections can not be calculated analytically. Instead, Monte Carlo generators are used to simulate these interactions. They usually use QCD-inspired models which contain free parameters that can be tuned such that the Monte Carlo prediction matches the experimental observations. Distributions of the primary charged-particles multiplicity (n_{ch}) can be used to constrain these parameters. The primary charged-particles multiplicity is defined as the number of primary charged particles that are produced in a *pp* collision. Especially interesting are n_{ch} distributions for various collision energies. They provide insights in the relative contributions soft and hard scattering since the latter will increase with the energy. Until now n_{ch} was measured for center-of-mass energies of up to 13.0 TeV [1–11]. The Minimum Bias (MinBias) analysis aims to measure the primary charged-particles multiplicity for 13.6 TeV.
The data for the analysis was taken at the ATLAS detector in a special run with a reduced average pile-up of only 0.005, so that the occurrence of multiple primary vertices at the same time is rare. This is necessary because n_{ch} is a per-event quantity and any ambiguities about the origin of a track due to pile-up would hinder the measurement. The trigger used for this analysis is based on the Minimum Bias Trigger Scintillators. It is able to select events even if they have just a single track. The measured n_{ch}-distributions are affected by the following efficiencies:

Trigger Efficiency The trigger used to select the events will miss some events with $n_{\mathrm{ch}} \geq 1$. The fraction of events that is detected is called the trigger efficiency ($\varepsilon_{\mathrm{trig}}$). It depends on the number of charged particles and is measured in data using a randomly seeded control trigger. To account for this, each event is weighted by the inverse trigger efficiency.

Vertex Reconstruction Efficiency Some vertices will not be reconstructed by the vertex finding algorithm. The rate of vertices that is detected is called the vertex reconstruction efficiency ($\varepsilon_{\mathrm{vtx}}$). Each event is weighted by the inverse vertex efficiency measured in data.

Track Reconstruction Efficiency The efficiency with which the tracking algorithm reconstructs tracks is called the track reconstruction efficiency ($\varepsilon_{\mathrm{trk}}$). Each track is weighted by the inverse tracking efficiency to account for this. The tracking efficiency is calculated from Monte Carlo (MC) simulations. For this, an accurate description of the material in the detector is needed. This is given for most detector regions but not all. In the regions where the material is not known with the required precision, data-driven methods like the Track-Extension-Efficiency-Method can be used to obtain the material profile and correct the tracking efficiency accordingly [12].

This thesis investigates multiple effects on the MinBias analysis related to the trigger performance and the track reconstruction. It starts with a description of the ATLAS detector at the LHC in Section 2 and an overview over the MinBias analysis in Section 3. Then, the performance of the MBTS is evaluated with respect to the activity of the modules as well as its timing ability in Section 4. In Section 5, the trigger efficiency is measured and systematic uncertainties to it are discussed. It is compared to the trigger efficiency measured in Run 2. Furthermore, in Section 6, the rate of beam background among the selected events is estimated using two different methods.

As a second topic the tracking efficiency is discussed with a focus on the description of the material between the Pixel Detector and the Semi-Conductor Tracker in Section 7. The amount of material in this region is estimated using the track extension efficiency. A correction to the tracking efficiency is then calculated based on the material estimate.

Finally, the results are summarized in Section 8 and an outlook is given.

2 The ATLAS Detector at the LHC

The Large Hadron Collider (LHC) is a circular particle collider that provides high-energy proton-proton collisions. The main collider ring has a circumference of 27 km. It holds two beams travelling in opposite direction. Each beam consists of bunches of about 10^{11} protons. These bunches are grouped into bunch trains. The bunches in each bunch train are closely following each other with a separation of approximately 25 ns.

The beams are brought to collision inside the different experiments located at the LHC. When two bunches collide at the interaction point of an experiment, this is called a paired bunch crossing. However, depending on the beam configuration it is also possible that only one bunch passes the interaction point while no bunch from the other beam is present. This is then called an unpaired bunch crossing. Unpaired bunch crossings are typically not the main interest of physics analyses but they can be used for example to study beam background.

The rate R of proton-proton events in paired bunch crossings can be calculated with the luminosity L:

$$R = \sigma L \tag{1}$$

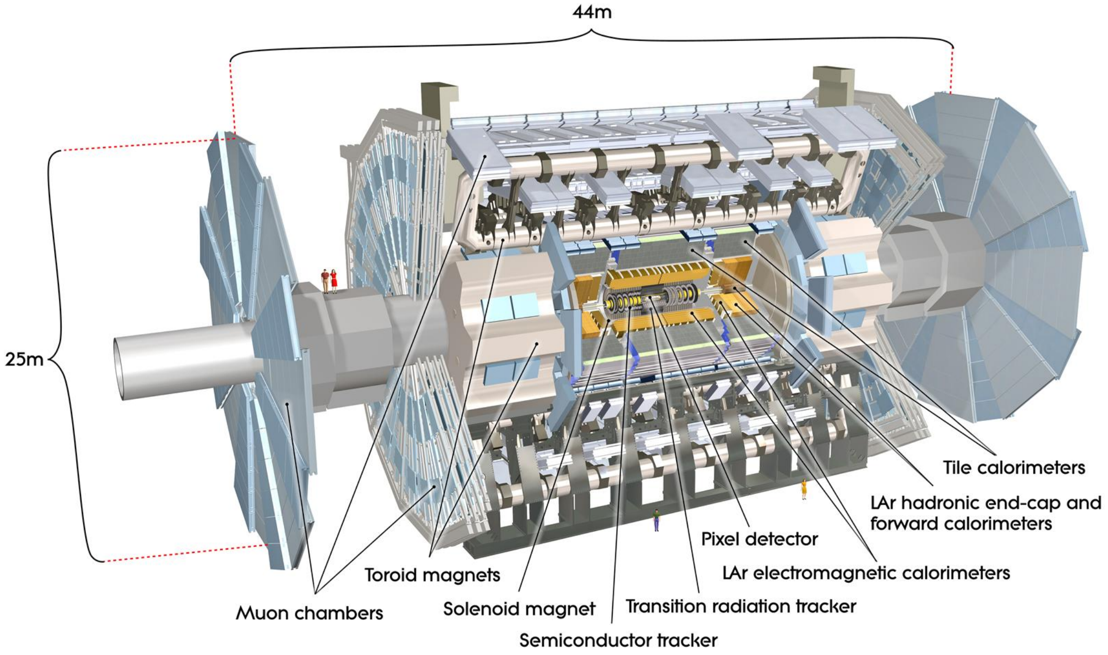

Figure 1: Schematic of the ATLAS detector. Taken from [14].

Here, the cross-section σ describes the fundamental probability of two protons colliding, while the luminosity encompasses the number of protons per bunch, the frequency of bunch crossings and focusing of the beams. The LHC can produce peak luminosities of about 2×10^{34} cm^{-2}s^{-1} [13]. However, it is also able to provide much lower luminosities for special runs. The number of pp-collision events per bunch crossing is called pile-up, denoted with μ. At high luminosities the average pile-up $\langle\mu\rangle$ will assume values of up to 57 [13].
Most studies rely on high luminosity and high pile-up data to obtain the required statistics. However, pile-up also makes it difficult to reconstruct the tracks, as the combinatorics increase and there is always some ambiguity about the tracks origin. Therefore, for some analyses, the luminosity and thus the pile-up is reduced to obtain datasets containing mostly single-collision events.

The ATLAS detector is a general purpose detector located at the LHC. A schematic of the ATLAS detector is shown in Fig. 1. The coordinate system of the ATLAS detector is centered around the nominal interaction point. The z-axis is aligned with the LHC beam pipe. The x-axis points from the interaction point (IP) towards the center of the LHC and the y-axis points upwards. Alternatively, when polar coordinates are used, $\phi = 0$ points upwards (i.e. in y-direction) and $\theta = 0$ points in z direction. Often the pseudo-rapidity η is used instead of θ. It derives from θ as follows:

$$\eta = -\ln\tan(\theta/2) \tag{2}$$

The positive hemisphere of the ATLAS detector is called A-side and the negative one is called C-side.

The ATLAS detector consists of multiple sub-detector systems which are located in concentric layers around the beamline. From innermost to outermost these are:

The Inner Detector The Inner Detector (ID) is a detector which allows to measure the tracks of charged particles. It covers an η region from -2.5 to 2.5. The ID is immersed in a 2 T magnetic field pointing in beam direction. Therefore, charged particles follow a helical trajectory whose curvature can be used to determine the particles momentum. Additionally, the ID is able to locate the vertex where the interaction occurred that created the particle.

Calorimeter System The Calorimeter System consists of the Electromagnetic Calorimeter and the Hadronic Calorimeter. The Electromagnetic Calorimeter is a lead - liquid argon sampling calorimeter which covers the range $|\eta| < 3.2$. Charged particles and photons that enter the Electromagnetic Calorimeter cause an electromagnetic shower and the resulting particles deposit energy in the liquid argon sampling layers. From this, the energy of the original particle can be reconstructed. The Forward Calorimeter extends the region in which electromagnetic calometry is possible up to $|\eta| < 4.9$.

The Hadronic Calorimeter comprises the Tile Calorimeter, which spans $|\eta| < 1.7$ and is made out of steel plates and scintillating plastic tiles, and the Hadronic End-Cap Calorimeter covering $1.5 < |\eta| < 3.2$, which is a copper - liquid argon calorimeter. Strongly interacting particles will form hadronic showers in the Hadronic Calorimeter which again deposit energy there. This allows to measure the energy of the incident particle. The hadronic part of the Forward Calorimeter extends the coverage of the hadronic calorimetry up to $|\eta| < 4.9$. [14]

Muon System Muons are mostly invisible to the calorimeters because they do not interact strongly and emit hardly any bremsstrahlung which is a prerequisite for the formation of an electromagnetic shower. To nevertheless measure the energy and momentum of muons, the muon system was built around the calorimeters. Three toroid magnets of eight coils each provide a magnetic field of up to 3.5 T in the Muon System region. Then, three layers of tracking chambers provide a measurement of the muon momentum, which is even improved when ID tracking information is included. The tracking chambers cover an η-range of -2.7 to 2.7. An additional trigger chamber allows to trigger on muons. The whole ATLAS

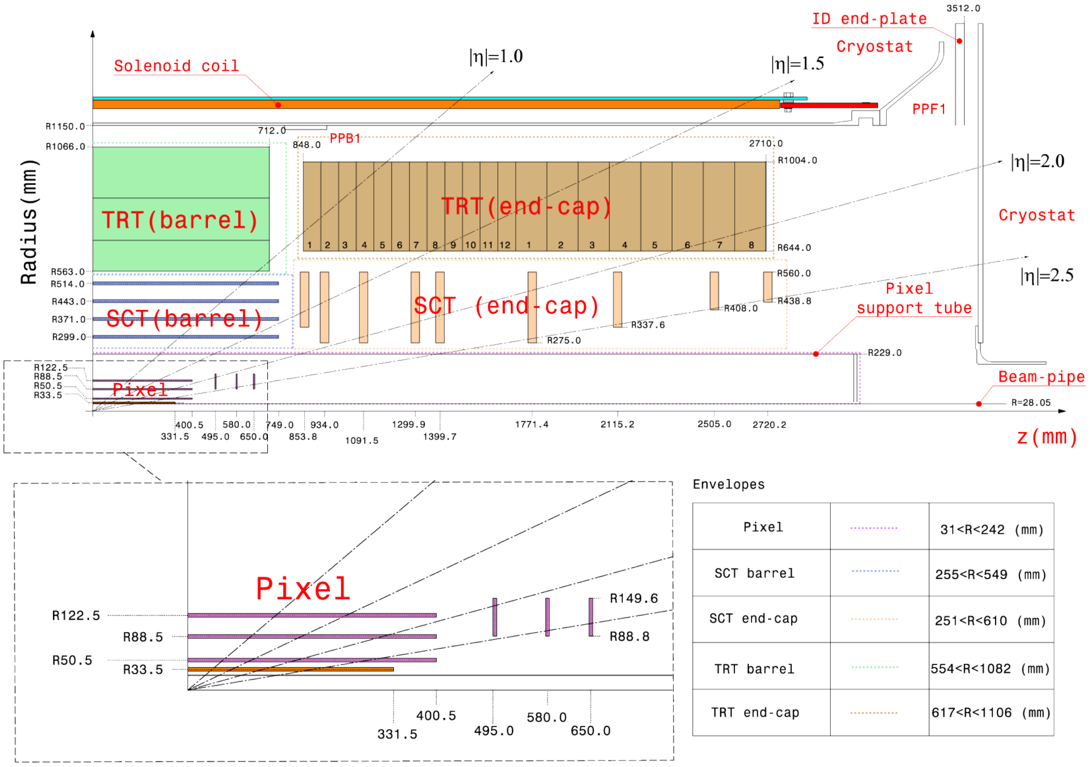

Envelopes

Pixel	┈	31<R<242 (mm)
SCT barrel	┈	255<R<549 (mm)
SCT end-cap	┈	251<R<610 (mm)
TRT barrel	┈	554<R<1082 (mm)
TRT end-cap	┈	617<R<1106 (mm)

Figure 2: Layout of the ID. Shown is the cross section through the r-z-plane. Taken from [15].

Muon system was designed with the goal to minimize material in order to avoid multiple scattering events.

Further information on all detector systems can be found in references [13] and [14].

The following sections highlight the regions and systems of the ATLAS detector that are especially important for this thesis.

2.1 Inner Detector

The measurement of n_{ch} conducted by the MinBias analysis relies exclusively on the ID because it only measures charged particles by default. Additionally, it is possible to exclude secondary particles due to its vertexing and tracking ability.

The ID is a tracking detector covering the range of $|\eta| < 2.5$ for all angles in ϕ. A schematic of the ID can be seen in Fig. 2. It consists of three sub-detector modules. The innermost module is the Pixel Detector, followed by the Semi-Conductor Tracker (SCT) and the outermost module is the Transition Radiation Tracker (TRT).

The Pixel Detector consists of four horizontal layers of pixel sensors (i.e. layers parallel to the beam pipe) and three vertical layers (i.e. perpendicular to the beam pipe). The closest layer to the beam pipe is at $r = 33.25\,\mathrm{mm}$, the farthest one is at $r = 122.5\,\mathrm{mm}$. The Pixel Detector is especially important for vertex finding because it is the closest detector to the beamline. It also has the best spacial resolution out of all three ID modules.

The SCT features four horizontal and nine vertical double-layers silicon microstrip detectors. Each double-layer consists of two single-sided silicon microstrip detectors with a stereo angle of 40 mrad. The SCT spans a range in r of 299 mm to 560 mm. It offers high granularity tracking in a wide area with less material per point than the Pixel Detector and at lesser costs.

The TRT consists of 73 horizontal and 160 vertical layers of straw tubes interleaved with transition radiation material. It spans a range in r of 563 mm to 1066 mm. The transition radiation material increases the energy deposition from low-mass particles. This is especially useful to discriminate electrons from other particles.

2.1.1 Tracks

On its way through the ID, a particle deposits energy in the different sub-detectors. The particles trajectory must therefore be reconstructed from the different detector signals. A reconstructed trajectory is called track. The track reconstruction algorithm fits tracks to the detector signals using combinatorial Kalman filters [16]. Then, an adaptive vertex finder determines the primary vertex of the event, i.e. the point of the primary scattering. For each track, the origin of the track is the point of closest approach to the beam line. If no primary vertex is found, the IP is used instead of the primary vertex to determine the origin.

In the solenoidal magnetic field which is present in the ID, charged particles follow a helical trajectory that can be fully parameterized by the following five parameters:

- The transverse momentum p_T of the corresponding particle which can be reconstructed using the tracks curvature in the magnetic field. It is the projection of the tracks momentum p onto the x-y-plane.
- The azimuthal angle φ of the particles trajectory at the origin where $\varphi = 0$ describes a track that points upwards (i.e. in y-direction).
- The pseudo-rapidity η of the particle at the origin or the corresponding polar angle θ.
- The transversal impact parameter d_0 which describes the distance of the trajectory from the measured beam line.
- The longitudinal impact parameter z_0 which describes the origins offset in z-direction with respect to the primary vertex or the beam spot if no primary vertex is found.

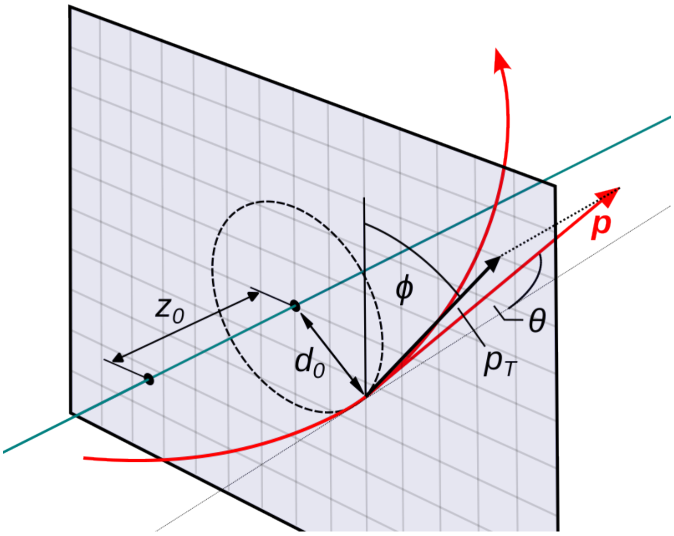

Figure 3: Illustration of the five geometrical track parameters. Beam line in blue, the plane is the x-y plane. The reconstructed track (red) does not enter the cylinder around the beam line that is indicated by the dashed circle. Figure made by author.

An illustration of these parameters is given in Fig. 3.
Other important variables are the number of hits in each detector sub-module that are associated with the track as well as the χ^2-value and the number of degrees of freedom of the tracks fit.

2.1.2 PP0 Region

The Pixel Detector relies on various cables, cooling pipes and support trays. Together these are called Pixel Services. Between Run 1 and Run 2 some of the pixel services were upgraded and relocated to areas further away from the interaction point in order to reduce the radiation dose and allow easier maintenance access. The region where these changes occurred is the so-called Patch Panel 0 (PP0) region, which is located between the Pixel Detector and the SCT at $|\eta| > 1.5$. The PP0 region contains many small parts with higher material density and composition in terms of Z. The material distribution used in simulations, however, contains averaged values for material density and composition. The exact material distribution in this area is hard to model and must be studied using data-driven methods.

2.2 MBTS

The Minimum Bias Trigger Scintillators (MBTS) are used as a trigger for the MinBias analysis. They consist out of two identical disks with 16 plastic scintillator

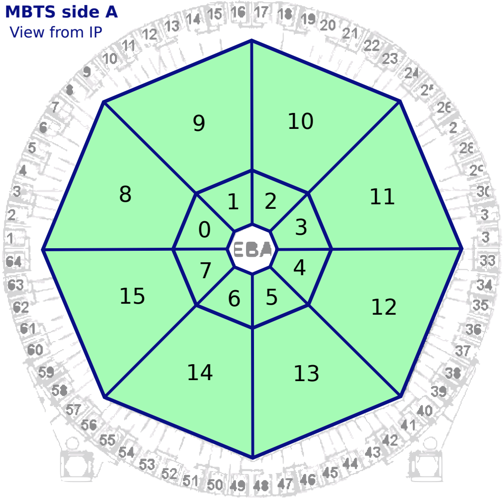

Figure 4: Layout of the MBTS. Each module is labeled with its respective ID-number. Adapted from [18].

modules each. The disks are located at the inner face plates of the electromagnetic endcap calorimeters at $z = \pm 3560\,\text{mm}$ and are perpendicular to the beam line. They cover an η-region of $2.1 < |\eta| < 3.8$ [17]. Both disks have an inner ring and an outer ring which are divided into 8 scintillator modules each. Each scintillator module is assigned a unique ID-number. The mapping is shown in Fig. 4.

Each module is connected to a photomultiplier tube which converts the scintillation light to an electric signal. This signal is then processed by a constant-fraction-discriminator to provide a fast triggering signal. Each stored event contains information about the charge deposited in each module and the time of the trigger signal of each module relative to the closest bunch crossing time provided by the LHC clock.

The MBTS modules used in Run 2 were made from the scintillating material UPS-923A. They degraded during Run 2 due to the exposition to radiation. Fig. 5 shows a degraded MBTS module from the inner ring. The degradation is located mainly

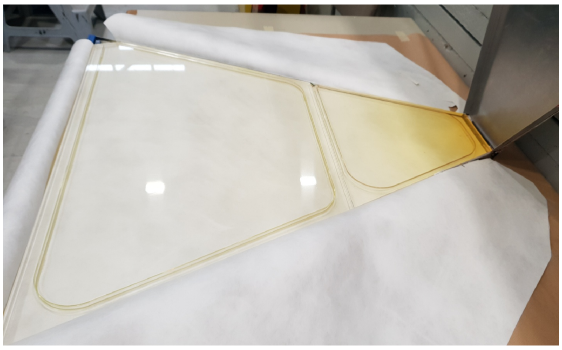

Figure 5: Inner Ring MBTS module from Run 2. The radiation damage inflicted during Run 2 shows as yellow discoloration and is primarily located in the area closest to the beam line. Taken from [19].

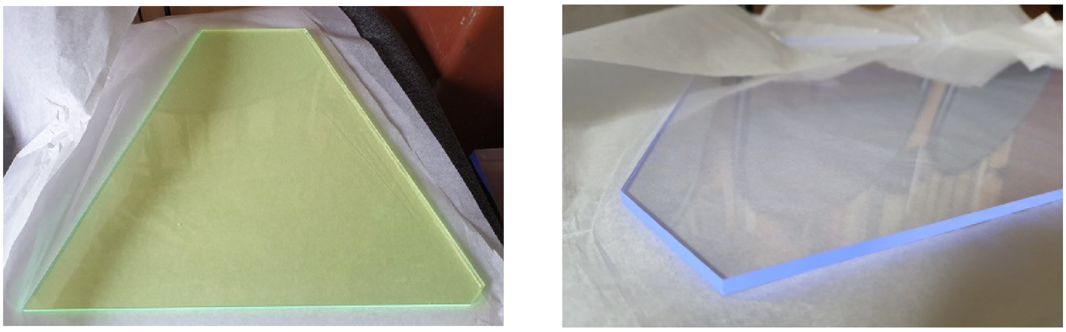

Figure 6: Inner MBTS green plate made from PS+BBQ (left) and Outer MBTS blue plate made from PS+PTP+POPOP (right). Taken from [17].

in the region close to the beamline of the inner ring modules. Therefore, in Run 3, a more radiation-hard green scintillator (PS+BBQ) was used for the inner modules whereas the outer modules were made of a blue scintillator (PS+PTP+POPOP) [17]. An example of one inner and one outer ring module can be seen in Fig. 6.

2.3 Trigger System

The number of events that can be stored by the ATLAS detector is limited by the bandwidth of the data acquisition system and the disk space of the storage facilities. Therefore, the ATLAS detector has a trigger system that makes live decisions on which events to save. These decisions are made in a two-step process: All events are first filtered by the hardware-based Level 1 Trigger (L1), which performs a quick pre-selection of events. The events accepted by the L1 are then passed to the software-based High-Level Trigger (HLT), which makes the final decision on which events to store permanently.

The L1 reduces the stream of events from approximately 40 MHz to about 100 kHz with a latency of less than 2.5 µs. The events selected by the L1 are then passed on to the HLT alongside with information on the Region of Interest that should be reconstructed by the HLT. The HLT reduces the event rate down to about 1.0 – 1.5 kHz with a decision time of less than 200 ms. Only those events that satisfy the conditions for at least one trigger at HLT-level are stored permanently. The information which L1-triggers and HLT-level triggered for each of these events is also stored.

To save bandwidth, a trigger can run on a so-called prescale. This means that only a fraction of the events satisfying the trigger conditions are selected. For each of these events, the probability to be selected is one over the prescale. For example, if the prescale of a trigger is 100, then every event that meets the requirements has a 1 % chance of actually being selected. Prescales can be applied both at L1 and at the HLT.

Nickname	Selection Algorithm		Prescale	
	L1	HLT	L1	HLT
MBTS_A	`MBTS_A`	`noalg_mb`	1	1
MBTS_C	`MBTS_C`	`noalg_mb`	1	1
signal	`MBTS_1`	`noalg_mb`	1	1
control	`RD0_FILLED`	`mb_sptrk`	143.659	3.33333
background	`MBTS_1_UNPAIRED_ISO`	`mb_mbts`	100	1

Table 1: Overview of the different triggers used in this thesis and their respective algorithms and prescales.

The triggers used in this analysis and their respective prescales are listed in Table 1. They will be referred to by the nickname given in the table rather than their technical name. The signal trigger is the trigger which selects the events used for the MinBias analysis. It fires at L1 if any of the 32 MBTS modules fires at a paired bunch crossing. Its HLT algorithm `noalg_mb` approves all the events selected by L1 without any further checks. The control trigger is used to calculate the trigger efficiency of the signal trigger. It provides an alternative way to select events with at least one track that does not rely on the MBTS. Instead, it is based on the Pixel Detector and the SCT in conjunction with a track reconstruction run on the HLT. Its L1 trigger randomly selects events from paired bunch crossings. The HLT algorithm `mb_sptrk` then checks that at least two pixel hits with a time over threshold of at least 20 bunch crossings and at least three SCT hits are present. Furthermore, it runs a track reconstruction algorithm and requires at least one track with $p_T > 200\,\text{MeV}$ and $d_0 < 40\,\text{mm}$ where d_0 is calculated against the beam line. The triggers MBTS_A and MBTS_C are used to determine a systematic uncertainty of the trigger efficiency of the signal trigger. They fire at paired bunch crossings if any of the 16 modules on the respective side fires. Lastly, the background trigger allows to estimate the amount of beam background events that will trigger the signal trigger. Like the signal trigger, it requires at least one of the 32 MBTS modules to fire, but it only selects events from unpaired bunch crossings.

3 The Minimum Bias Analysis

QCD interactions in the low-energy non-perturbative region can not be calculated analytically but must instead be simulated by MC generators. They usually use QCD-inspired models which contain free parameters that can be tuned such that the Monte Carlo prediction matches the experimental observations. Distributions of the primary charged-particles multiplicity (n_{ch}) can be used to constrain these parameters. n_{ch} is defined as the number of primary charged particles with lifetimes

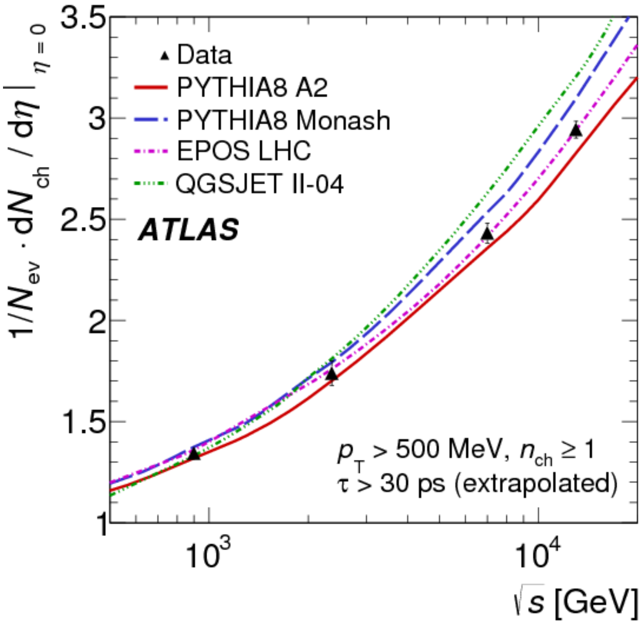

Figure 7: The average primary-charged-particle multiplicity in pp interactions per unit of pseudorapidity, η, for $|\eta| < 0.2$ as a function of the center-of-mass energy. Charged strange baryons are included in the definition of primary particles. The data are compared to various particle-level MC predictions. The vertical error bars on the data represent the total uncertainty. Taken from [11].

above 300 ps that are produced in a single pp collision. A particle is considered primary if it is either directly produced in the pp collision or if it is from the decay of a directly produced short-living particle with a lifetime of less than 30 ps. The other particles, i.e. those that are produced from the decay of particles with lifetimes above 30 ps, are called secondary particles. The threshold of 300 ps was chosen higher than 30 ps in order to exclude strange baryons which usually decay within the detector and therefore have low reconstruction efficiencies of approximately 0.3 % [11].

Especially interesting to the MinBias analysis is how various n_{ch} distributions change with the collision energy. These distributions provide insights in the relative contributions of soft and hard scattering since the latter will increase with the energy. A comparison of the primary charged-particles multiplicity at central η measured experimentally with the predictions of various MC generators is shown in Fig. 7. Until now n_{ch} was measured for center-of-mass energies of up to 13.0 TeV [1–11]. The MinBias analysis aims to measure primary charged-particles distributions at a collision energy of 13.6 TeV.

The phase space for this analysis is chosen to be $|\eta| < 2.5$ and $p_T > 500\,\mathrm{MeV}$ due to the acceptance of the ID. In principle the acceptance of the ID would allow for the p_T cut to be lowered to 100 MeV, however for consistency with older analyses the threshold is chosen to remain at 500 MeV.

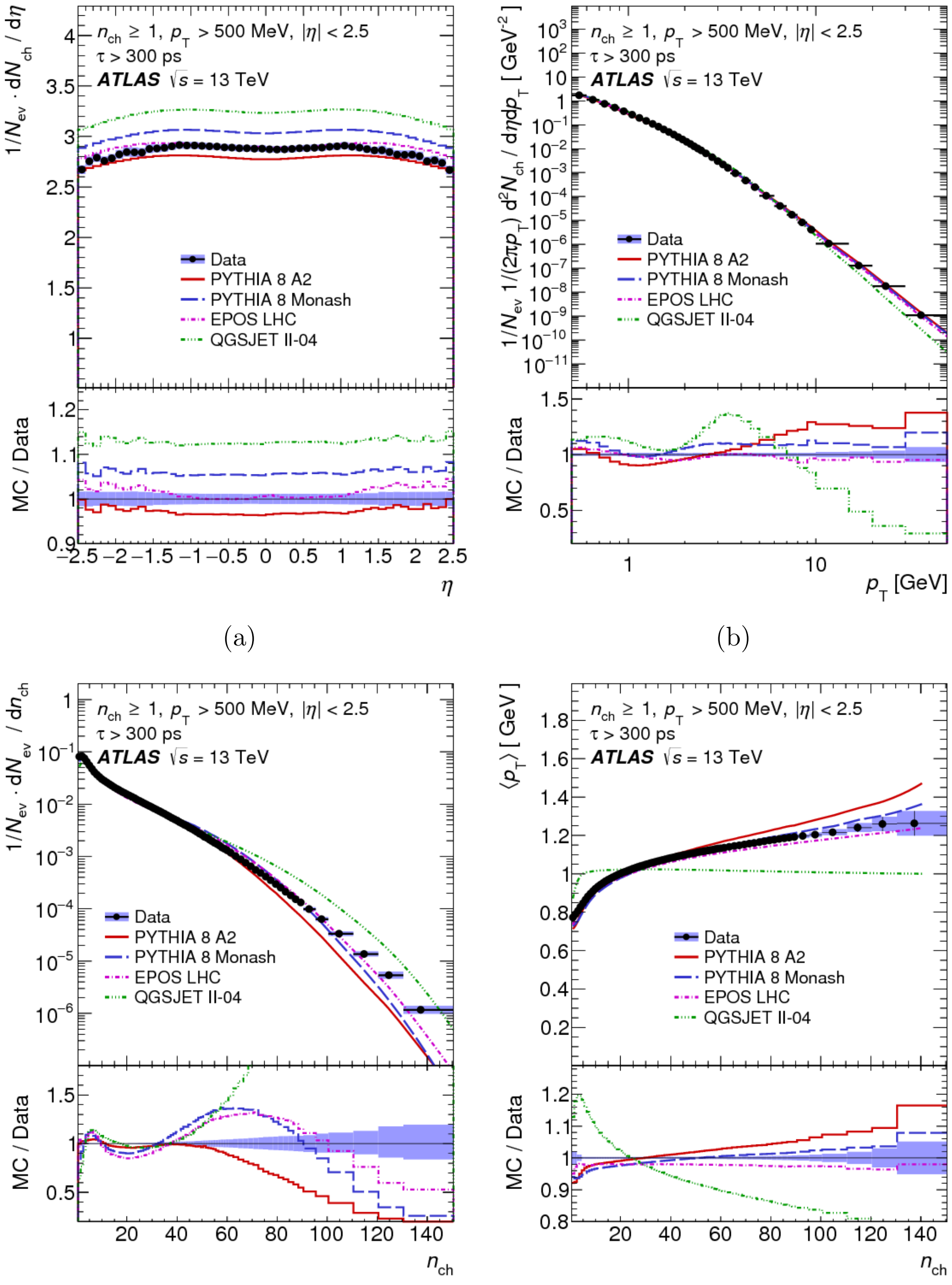

(a) (b)

(c) (d)

Figure 8: Primary-charged-particle multiplicities as a function of (a) pseudorapidity, η, and (b) transverse momentum, p_T; (c) the multiplicity, n_{ch}, distribution and (d) the mean transverse momentum, $\langle p_T \rangle$, versus n_{ch} in events with $n_{\text{ch}} \geq 1$, $p_T > 500\,\text{MeV}$ and $|\eta| < 2.5$. The dots represent the data and the curves the predictions from different MC models. The x-value in each bin corresponds to the bin centroid. The vertical bars represent the statistical uncertainties, while the shaded areas show statistical and systematic uncertainties added in quadrature. The bottom panel in each figure shows the ratio of the MC simulation over the data. Since the bin centroid is different for data and simulation, the values of the ratio correspond to the averages of the bin content. Taken from [11].

The following distributions are measured:

- $\frac{1}{N_{\mathrm{ev}}} \cdot \frac{\mathrm{d}N_{\mathrm{ch}}}{\mathrm{d}\eta}$
- $\frac{1}{N_{\mathrm{ev}}} \cdot \frac{1}{2\pi p_{\mathrm{T}}} \cdot \frac{\mathrm{d}^2 N_{\mathrm{ch}}}{\mathrm{d}\eta \mathrm{d}p_{\mathrm{T}}}$
- $\frac{1}{N_{\mathrm{ev}}} \cdot \frac{\mathrm{d}N_{\mathrm{ev}}}{\mathrm{d}n_{\mathrm{ch}}}$
- $\langle p_{\mathrm{T}} \rangle$ as a function of n_{ch}

Here n_{ch} is the primary charged-particles multiplicity for a single event as defined earlier and N_{ch} is the total number primary charged particles among all events. N_{ev} is the number of events with at least one primary charged particle ($n_{\mathrm{ch}} \geq 1$). The results of Run 2 at 13.0 TeV compared to the predictions from various MC generators are shown in Figs. 8a to 8d. The distributions highlight clear differences between MC models and the measured distributions. Among the models considered, EPOS [20] reproduces the data the best, PYTHIA 8 [21] with the A2 [22] and MONASH [23] tune give reasonable descriptions of the data, and QGSJET-II [24] provides the worst description of the data [11]. The MinBias analysis plans similar comparisons for the primary charged-particles distributions that will be measured at 13.6 TeV.

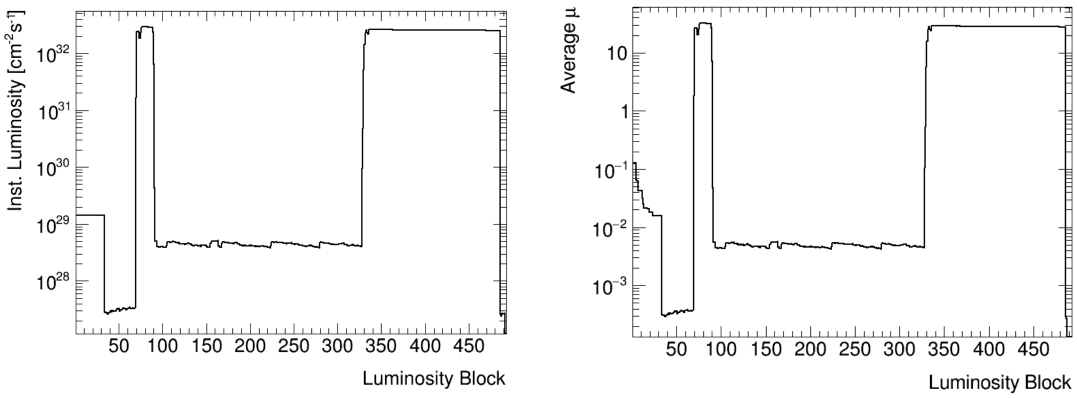

(a) Instantaneous luminosity

(b) Interactions per bunch crossing

Figure 9: Run 427929 characteristics per luminosity block. Data from [25].

3.1 Data Sample

For the MinBias analysis, all tracks in an event must come from the same *pp* interaction. Therefore, the data for the MinBias analysis is taken from the special low-μ run 427929. It has low beam currents and reduced beam focusing such that the expected mean number of interactions per bunch crossing $\langle \mu \rangle$ is only 0.005. That means, on average, there is only one collision per 200 bunch crossings, and it also means that out of 200 bunch crossings with a collision event, only one will include a second event. The actual mean number of interactions can be seen in Fig. 9b. For this analysis only luminosity blocks in the range from 119 to 324 are used.

To achieve such low $\langle\mu\rangle$ the luminosity must be reduced compared to a normal run. This can be seen in Fig. 9a. The shape of the luminosity curve matches $\langle\mu\rangle$. The total integrated luminosity of all the luminosity blocks used for this analysis is $0.445\,\mathrm{nb}^{-1}$.

For the estimation of the beam background, the bunch crossing structure of the beam is also important. The run had eight bunch trains of eight bunches each. The ratio of paired bunch crossings to unpaired bunch crossings was 64/16.

The events interesting for this analysis are those with at least one primary charged particle. Therefore, all tracks that satisfy the following criteria are selected:

- They are selected by the signal trigger (definition at Section 2.3).
- A primary vertex is reconstructed.
- No secondary vertex with four or more tracks is reconstructed (to exclude events where a second primary vertex was misclassified as a secondary vertex).
- The event contains at least one selected track as defined in the next section.

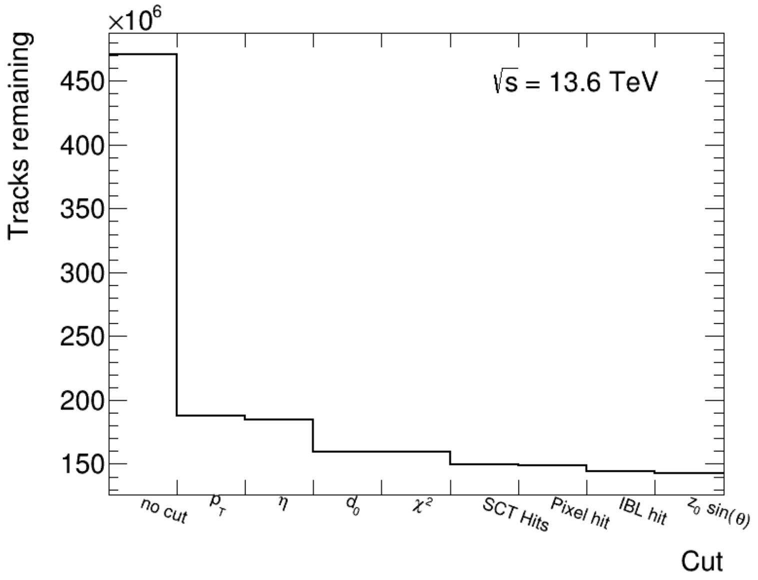

Figure 10: Remaining tracks after the named cut and all previous cuts are applied. The first bin shows all tracks from any signal event.

3.2 Track Selection

In order to select tracks from primary charged particles as defined above, the following track selection criteria are applied:

- $p_T > 500\,\mathrm{MeV}$
- $|\eta| < 2.5$
- $|d_0| < 1.5\,\mathrm{mm}$
- A χ^2-Probability of above 0.01 for tracks with $p_T > 10\,\mathrm{GeV}$
- At least one hit in the Pixel Detector and six hits in the SCT
- A hit in the innermost pixel layer, if a hit is expected, otherwise a hit in the next-to-innermost pixel layer. If no hit is expected in either of these layers the track is also selected.
- $|z_0 \sin(\theta)| < 1.5\,\mathrm{mm}$

The cuts on d_0 and z_0 are to exclude secondary particles. No cut on the charge is needed because the ID can only detect charged particles. To exclude mismeasured tracks, a χ^2 cut is performed for particles with high transverse momentum. For the hit requirements, if a particle passes through a dead module, it is counted as a hit. Fig. 10 depicts the remaining tracks as more cuts are applied successively. The number of selected tracks in a given event is called n_{sel}. It can be thought of as the number of primary charged particles as measured by the detector but it has to be weighted and unfolded to gain the actual value of n_{ch}.

For some measurements it is necessary to alter the selection criteria. When this is the case the changes will be given in the respective section of this thesis.

3.3 Monte Carlo Samples

Some quantities, for example the track reconstruction efficiency, are necessary for the measurement of the n_{ch} distributions but can not be determined using data alone. Instead, they are obtained from MC simulations. The MinBias analysis uses the following samples:

- The nominal sample contains 70 million events that were produced using the unmodified standard material distribution. It is the main sample that is used and all MC measurements use this sample unless otherwise stated.

- The so-called PP0 sample was produced using a modified material distribution where the density of the material in the PP0 region was increased by 25 %. It is used to estimate the material distribution in the PP0 region and its effect on the track reconstruction efficiency. The sample contains 270 million events.
- Some additional samples with material variations in other regions where the material distribution is better known are also produced to assess systematic uncertainties. In this thesis, however, they will not be used.

All samples were created using PYTHIA 8 [21] with the ATLAS minimum-bias tune A2 [22]. In addition, the samples are also produced with different generators and tunes to estimate systematic uncertainties. In this thesis, however, only the main samples produced with PYTHIA 8 and the A2 tune will be used.

3.4 Unfolding

The quantities measured by the detector will differ from the truth due to various detector effects. Therefore, the four distributions measured by the MinBias analysis are unfolded according to the following procedure: First, the events and tracks are weighted to account for various detector effects and for particles that are mistakenly included in the measurement. Then, a Bayesian unfolding is applied to the multiplicity distribution and to the distribution of $\langle p_T \rangle$. Finally, the distributions are again normalized according to the new value of N_{ev} after the unfolding.
Each event is weighted according to the following formula:

$$w_{\mathrm{ev}}(n_{\mathrm{sel}}, \eta) = \frac{1}{\varepsilon_{\mathrm{trig}}(n_{\mathrm{sel}})} \cdot \frac{1}{\varepsilon_{\mathrm{vtx}}(n_{\mathrm{sel}}, \eta)} \tag{3}$$

$\varepsilon_{\mathrm{trig}}(n_{\mathrm{sel}})$ is the efficiency of the signal trigger that is applied to account for the fact that the signal trigger will miss some events with $n_{\mathrm{ch}} \geq 1$. $\varepsilon_{\mathrm{vtx}}(n_{\mathrm{sel}}, \eta)$ is the efficiency of the vertex finding algorithm which also might miss some vertices. The event weight is relevant for all four distributions measured by the MinBias analysis.
The tracks are weighted by the following formula:

$$w_{\mathrm{trk}}(p_T, \eta) = \frac{1 - f_{\mathrm{sec}}(p_T, \eta) - f_{\mathrm{sb}}(p_T) - f_{\mathrm{okr}}(p_T, \eta)}{\varepsilon_{\mathrm{trk}}(p_T, \eta)} \tag{4}$$

$f_{\mathrm{sec}}(p_T, \eta)$ is the fraction of secondary tracks among the selected tracks that are not filtered out by the selection criteria. It is obtained by fitting MC-generated templates of primary and secondary particles to the data. $f_{\mathrm{sb}}(p_T)$ is the fraction of strange baryons among the selected tracks as calculated from MC simulations.

$f_{\mathrm{okr}}(p_T, \eta)$ is the fraction of tracks that are outside the kinematic range and only appear to be inside due to imperfect detector resolution. It is also calculated using MC simulations. The track weight is applied to the η and p_T distributions of N_{ch} as well as the distribution of $\langle p_T \rangle$.

4 MBTS Performance

The signal trigger relies on the MBTS. Therefore, the performance of the MBTS is tested with various measurements presented in this section.

4.1 Module Response

Due to the symmetry of the ALTAS detector, all inner MBTS modules are expected to fire with the same probability as all other inner modules, and all outer modules are expected to fire with the same probability as all other outer modules. Therefore, Fig. 11 shows for how many signal events with at least one selected track each module has registered a charge deposition of at least 0.01 pC. This is approximately the threshold where a module triggers the signal trigger. All modules but two show similar rates. Modules 13 and 17 fire much less. They are located on the outer A-side and the inner C-side respectively. Their position is marked in Fig. 12.

Each MBTS module also has a timing ability. A higher threshold of 0.18 pC is used for the timing. Therefore, the module response plot is also produced for this higher threshold. The result can be seen in Fig. 13. In addition to the two dead modules 13 and 17, also most of the inner A-side ring is less efficient than the other modules at the high threshold. The position of the dead and inefficient modules can be seen in Fig. 14. Here, all modules that fired less than three-quarters as often as the most efficient module are defined as inefficient.

4.2 MBTS Timing

The beam background can be identified using MBTS time information. It is therefore necessary to investigate the timing capabilities of the MBTS.

4.2.1 Time Multiplicity

The MBTS does provide time information only for a fraction of the modules that triggered. For a given event, the number of modules that provide time information is called time multiplicity. Fig. 15 shows a histogram of the time multiplicity of the signal events.

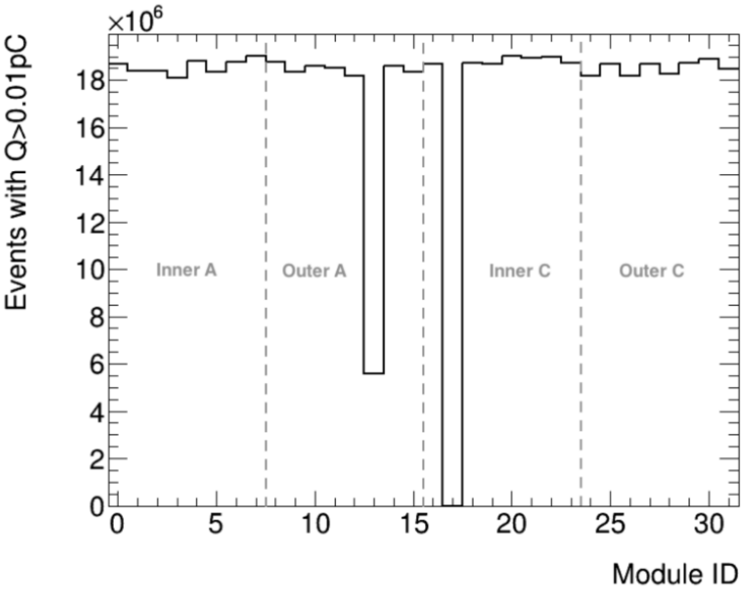

Figure 11: Number of signal events where an MBTS module registered a threshold of at least 0.01 pC. Modules 0-7 are the inner modules on the A-side, 8-15 are the outer ones. Modules 16-23 are on the inner C-side and modules 24-31 are on the outer C-side.

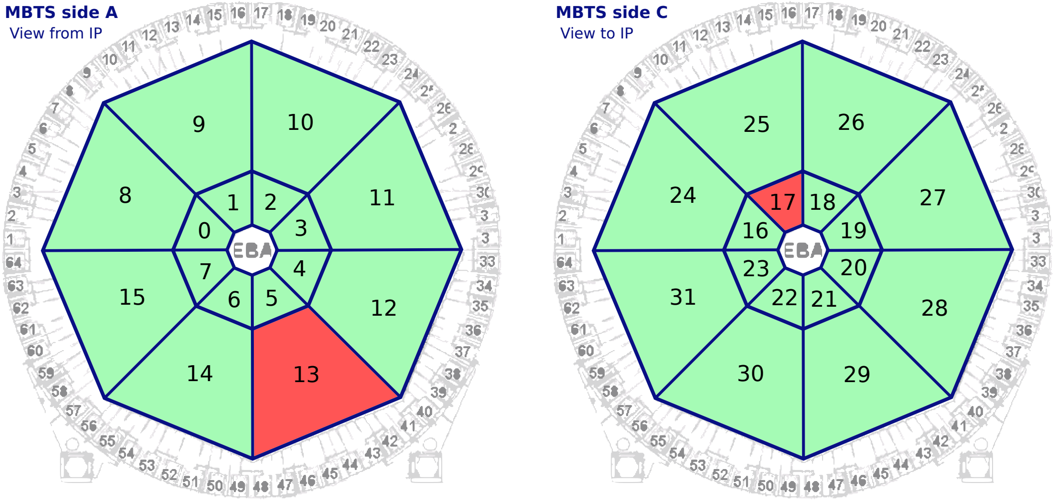

Figure 12: MBTS layout with modules marked in red that are dead at a threshold level of 0.01 pC.

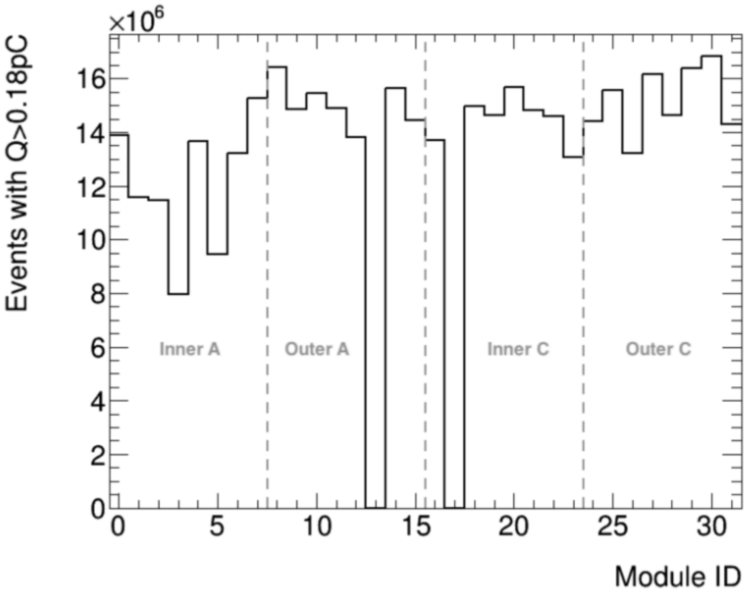

Figure 13: Number of signal events where an MBTS module registered a threshold of at least 0.18 pC.

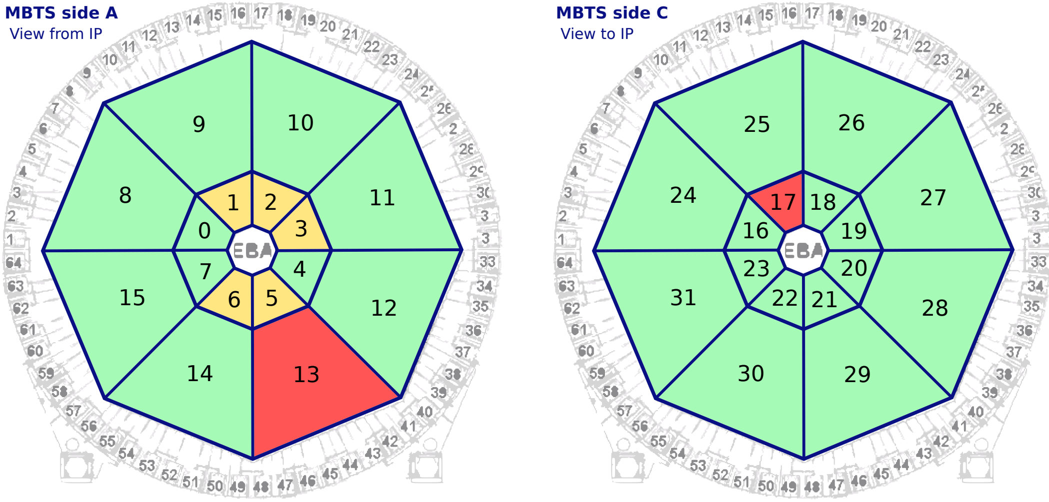

Figure 14: MBTS layout where modules that are dead/inefficient at a threshold level of 0.18 pC are marked in red/yellow.

Due to the two dead modules, the maximum time multiplicity measured was 30. The peak at 15 is due to beam background events, which typically trigger exactly one MBTS disk. Since both MBTS disks have exactly 15 working modules, the time multiplicity from beam background events peaks at 15.
For 8.0 % of all events, none of the modules provide time information, although at least one module must have triggered the event. Also, an additional measurement showed that only 66.7 % of all signal events in the run have time information on both sides. This means that for the remaining 33.3 % no time difference can be calculated.

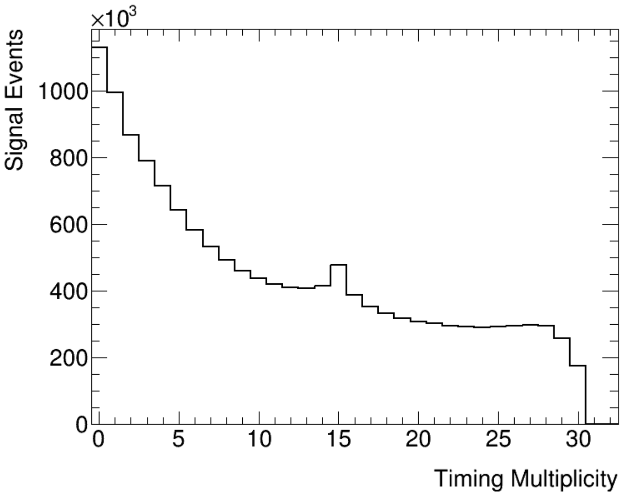

Figure 15: Number of MBTS modules with time information.

4.2.2 Time Calibration

When an MBTS module triggers, it provides a timestamp relative to the closest bunch crossing. To achieve this, a delay must be set for each module. During data collection, these delays were not configured properly, so the timestamps were not synchronized. This can be seen in Figs. 16a and 16b where the time distribution and mean time per module are shown, respectively. The mean times of the working modules span a wide range from −2.1 ns to 22.2 ns. Therefore, calibration of the times is necessary. Since no official calibration is available yet, the timestamps for each module are shifted by the module mean time as a preliminary calibration. For the dead modules, the mean time can not be properly calculated due to limited statistics. Therefore, their times remain unchanged. After this calibration, all working modules have the same mean time as can be seen in Figs. 16c and 16d. In all subsequent chapters, only the calibrated times are be used.

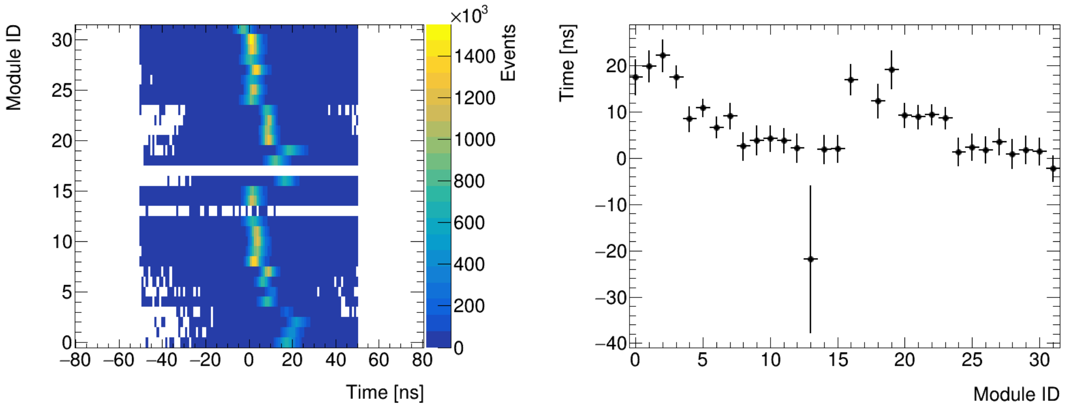

(a) Uncalibrated Distribution (b) Uncalibrated Mean Times

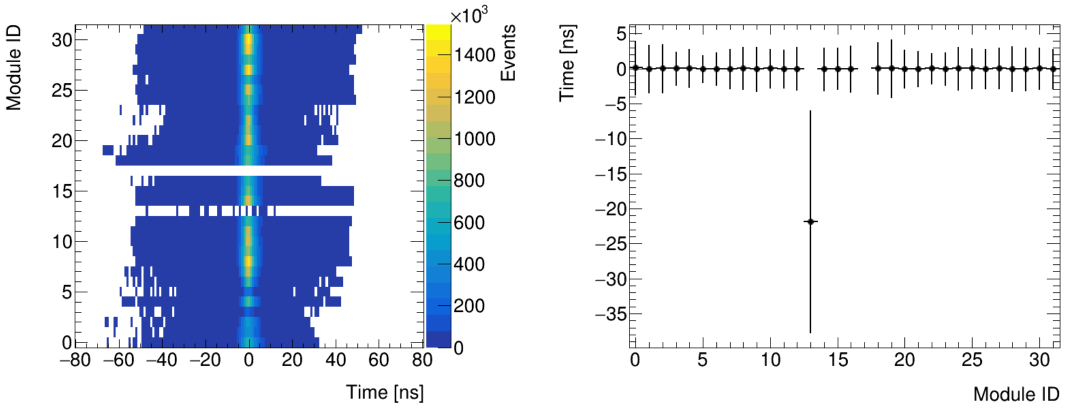

(c) Calibrated Distribution (d) Calibrated Mean Times

Figure 16: Time distribution per MBTS module and the modules mean times calculated in the range of ± 5 bins around the maximum bin for times before (Figs. a,b) and after calibration (Figs. c,d). The error bars indicate the standard deviation of the time distribution for this module.

5 Trigger Efficiency Studies

For the MinBias analysis all events with $n_{\text{sel}}^{\text{no-z}} \geq 1$ need to be selected. This is done using the signal trigger (definition at Section 2.3). To measure its performance, a sample of randomly selected events with at least one track is used. This sample is provided by the control trigger (definition at Section 2.3). The trigger efficiency $\varepsilon_{\text{trig}}$ is the fraction of events in this sample which are also selected by the signal trigger:

$$\varepsilon_{\text{trig}} = \frac{\text{control fired \&\& signal fired}}{\text{control fired}}$$

The control trigger is chosen because it ensures that all events in the control sample have at least one track and should therefore be selected by the signal trigger as well. Furthermore, the control trigger relies on the ID which covers $|\eta| < 2.5$ while the signal trigger uses the MBTS in the region $2.09 < |\eta| < 3.84$. Since

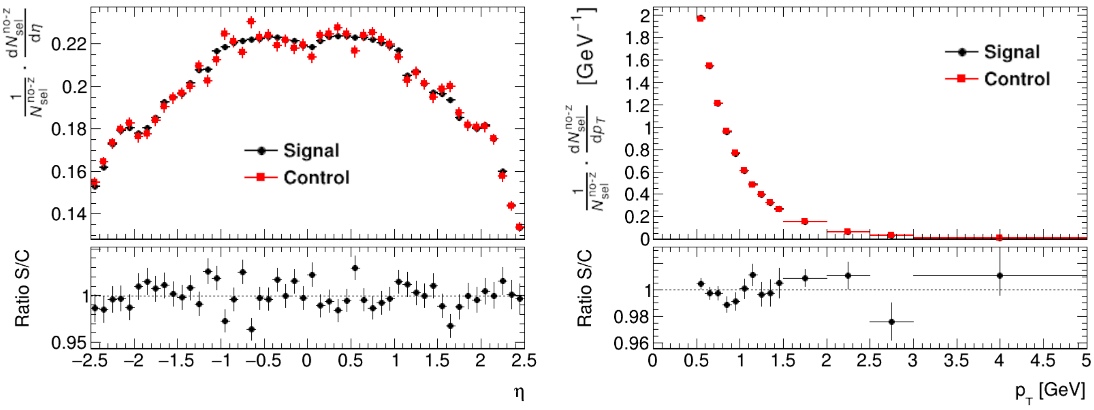

(a) η-distribution

(b) p_T-distribution

Figure 17: η- and p_T-distributions of the tracks normalized by the total number of selected tracks for signal events (black) and control events (red). The lower panels of each plot show the ratio of the signal distribution divided by the control distribution.

these regions have only a small overlap, the correlation between control and signal trigger is minimized.

The trigger efficiency and the vertex reconstruction efficiency are independently measured and corrected for. Therefore, in this section, none of the event selection criteria described in Section 3.1 are applied, as they rely on the reconstruction of vertices and would therefore introduce a dependency between the two quantities. In general, the more tracks there are, the more likely an event will be detected. Therefore, the $\varepsilon_{\text{trig}}$ is measured as a function of the selected tracks, however, the cut on $|z_0 \sin(\theta)|$ is removed because it also depends on the reconstruction of a primary vertex. The number of selected tracks without the $|z_0 \sin(\theta)|$ cut is called $n_{\text{sel}}^{\text{no-z}}$.

5.1 Investigation of possible Control Trigger Biases

The trigger efficiencies of the signal and the control trigger are dependent on the η- and p_T-values of the tracks in an event. If this spatial dependency differs between the two triggers, certain η-p_T-regions will be overweighted in the efficiency calculation while others will be underweighted. Therefore, the η and p_T distribution of the two triggers are compared.

Fig. 17a shows the number of selected tracks per η-bin. To make the two distributions comparable even though the control trigger is prescaled, each distribution is normalized by the total number of selected tracks $N_{\text{sel}}^{\text{no-z}}$. In most bins, the two distributions agree within uncertainties. Therefore, no bias due to the η-distribution is assumed.

Fig. 17b shows the number of selected tracks per p_T-bin normalized by $N_{\text{sel}}^{\text{no-z}}$.

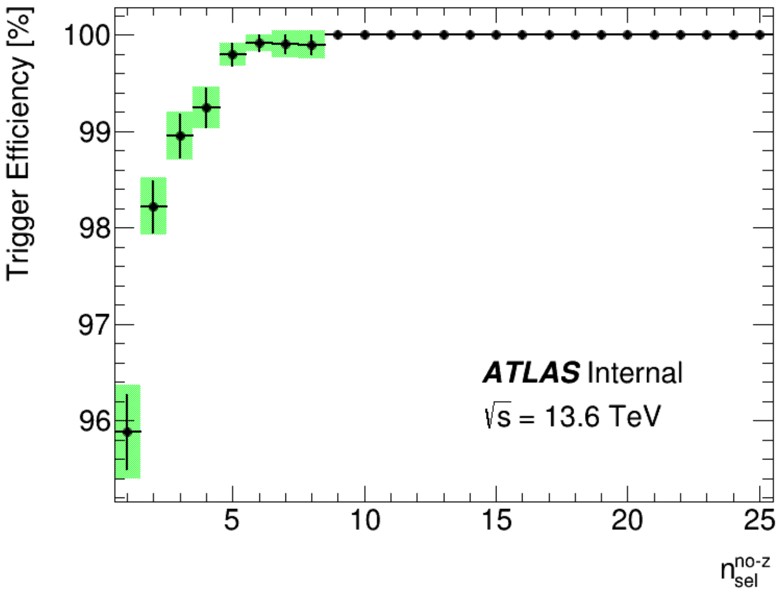

Figure 18: Trigger efficiency of the signal trigger. Systematic uncertainties are indicated by the error bars and combined statistical and systematic uncertainties are given by the green boxes.

The number of selected tracks is rapidly falling with p_T. Therefore, a variable binning with larger bin sizes for higher p_T is used. Again, the distributions agree reasonably well, so no bias due to the p_T-distribution is assumed.

5.2 Trigger Efficiency

Fig. 18 depicts the measured trigger efficiency. It is $(95.9 \pm 0.5)\,\%$ for events with one selected track and then continues to grow until it reaches $100\,\%$ for events with at least 9 selected tracks.
That is worse than the trigger efficiency measured in Run 2, which was $(98.9 \pm 0.5)\,\%$ for events with one selected track [11]. This can be explained by the fact that two out of 32 MBTS counters were dead (see Section 4.1).

5.3 Systematic Uncertainties

In this section the different sources of systematic uncertainty of the trigger efficiency are discussed.

5.3.1 Selection Uncertainty

To evaluate the uncertainty of the trigger efficiency due to the track selection, the trigger efficiency is calculated for an alternate track selection. The cut on d_0 is removed and instead the cut $|z_0 \sin(\theta)| < 1.5\,\text{mm}$ is introduced. The differ-

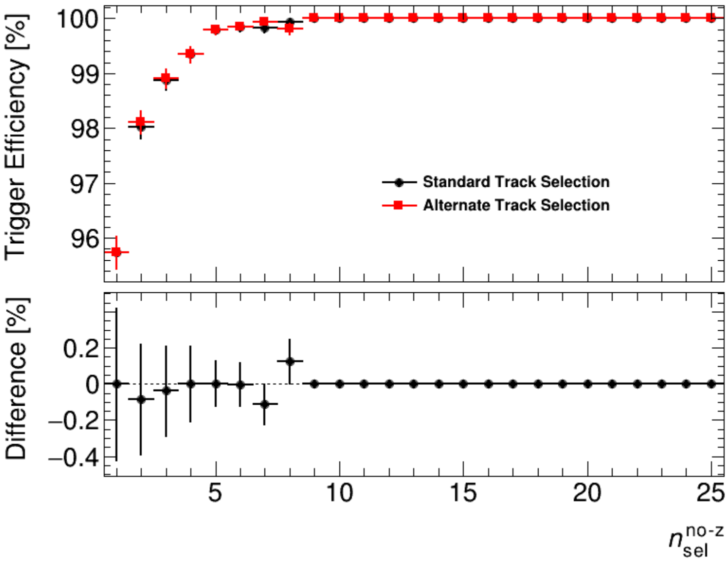

Figure 19: Trigger efficiency for both the standard track selection as well as the alternate track selection (without d_0-cut but with z_0-cut). The lower panel shows the difference between the two which is used as a systematic uncertainty of the trigger efficiency.

ence between the usual and the alternate track selection is taken as a systematic uncertainty of the trigger efficiency.

The addition of the cut on $|z_0 \sin(\theta)|$ means that more tracks are rejected, causing events to migrate towards bins with fewer tracks. The removal of the d_0 cut has the opposite effect. It shifts events towards bins with more tracks. Therefore, the combination of the two was chosen so that events migrate in both directions.

The trigger efficiencies for both track selections, as well as their difference, can be seen in Fig. 19. Although the two efficiencies match within the statistical uncertainties, their difference still is used as a systematic uncertainty of the trigger efficiency. The uncertainties obtained this way are consistently below 0.11 %.

5.3.2 Non-Uniform Response

To estimate the systematic uncertainty of the trigger efficiency due to the choice of the control trigger one would like to choose a different control trigger and compare the resulting trigger efficiency. However, no other suitable trigger was enabled during the data taking. Therefore, as a substitute, a systematic is derived from the difference between the trigger efficiencies measured using only the A-side ($\varepsilon_{\text{trig}}^{A}$) or only the C-side ($\varepsilon_{\text{trig}}^{C}$) of the MBTS. These efficiencies are obtained using the triggers MBTS_A and MBTS_C that are described in Section 2.3.

In principle, the trigger efficiency for one side $\varepsilon_{\text{trig}}^{\text{oneside}}$ should be the same irregardless of which side is chosen due to the symmetry of both the MBTS and the decay.

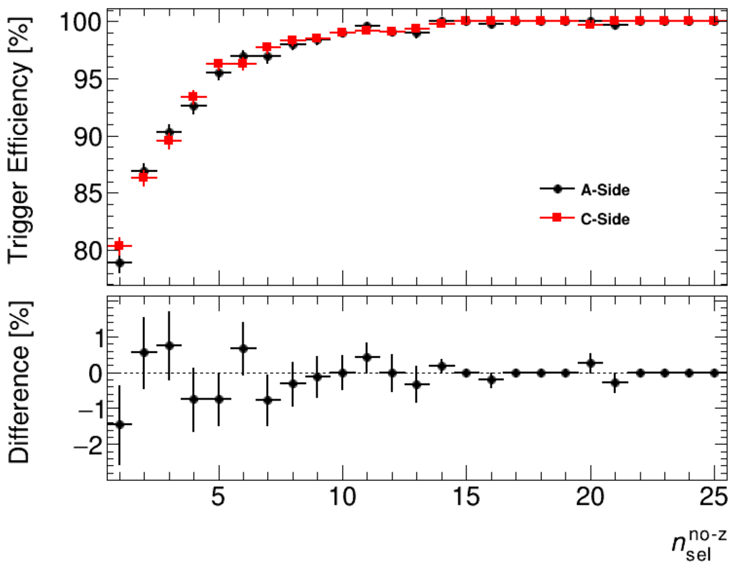

Figure 20: Trigger efficiency using only MBTS_A or MBTS_C respectively. The lower panel shows the difference between the two.

In practice, however, the trigger efficiencies for only A-side and only C-side will differ slightly. The systematic uncertainty is obtained by expressing the trigger efficiency in terms of $\varepsilon_{\mathrm{trig}}^{\mathrm{oneside}}$ and then propagating the uncertainty of $\varepsilon_{\mathrm{trig}}^{\mathrm{oneside}}$ to the trigger efficiency. The signal trigger fires if at least one side fires. Therefore, it derives from $\varepsilon_{\mathrm{trig}}^{\mathrm{oneside}}$ as follows:

$$\begin{aligned} \varepsilon_{\mathrm{trig}} &= \varepsilon_{\mathrm{trig}}^{\mathrm{oneside}} + (1 - \varepsilon_{\mathrm{trig}}^{\mathrm{oneside}})\varepsilon_{\mathrm{trig}}^{\mathrm{oneside}} \qquad (5) \\ &= 2\varepsilon_{\mathrm{trig}} - (\varepsilon_{\mathrm{trig}}^{\mathrm{oneside}})^2 \\ \Delta\varepsilon_{\mathrm{trig}} &= 2\Delta\varepsilon_{\mathrm{trig}}^{\mathrm{oneside}} - 2\varepsilon_{\mathrm{trig}}^{\mathrm{oneside}}\,\Delta\varepsilon_{\mathrm{trig}}^{\mathrm{oneside}} \qquad (6) \end{aligned}$$

Using $\varepsilon_{\mathrm{trig}}^{\mathrm{oneside}} = \frac{1}{2}(\varepsilon_{\mathrm{trig}}^{A} - \varepsilon_{\mathrm{trig}}^{C})$ and its corresponding uncertainty $\Delta\varepsilon_{\mathrm{trig}}^{\mathrm{oneside}} = \frac{1}{2}(\varepsilon_{\mathrm{trig}}^{A} - \varepsilon_{\mathrm{trig}}^{C})$ one obtains the systematic uncertainty of the trigger efficiency due to the non-uniform response of A- and C-side $\Delta\varepsilon_{\mathrm{trig}}^{\mathrm{non\text{-}uniform}}$:

$$\begin{aligned} \Delta\varepsilon_{\mathrm{trig}}^{\mathrm{non\text{-}uniform}} &= 2\Delta\varepsilon_{\mathrm{trig}}^{\mathrm{oneside}} - 2\varepsilon_{\mathrm{trig}}^{\mathrm{oneside}}\,\Delta\varepsilon_{\mathrm{trig}}^{\mathrm{oneside}} \\ &= (1 - \varepsilon_{\mathrm{trig}}^{\mathrm{oneside}})\left(\varepsilon_{\mathrm{trig}}^{A} - \varepsilon_{\mathrm{trig}}^{C}\right) \end{aligned} \qquad (7)$$

The trigger efficiencies for only MBTS_A and MBTS_C are depicted in Fig. 20. From the difference between these two, $\Delta\varepsilon_{\mathrm{trig}}^{\mathrm{oneside}}$ is calculated. The result can be seen in Fig. 21. The systematic uncertainty due to non-uniform response is largest in the first bin where it amounts to 0.3 %. It then decreases rapidly with $n_{\mathrm{sel}}^{\mathrm{no\text{-}z}}$.

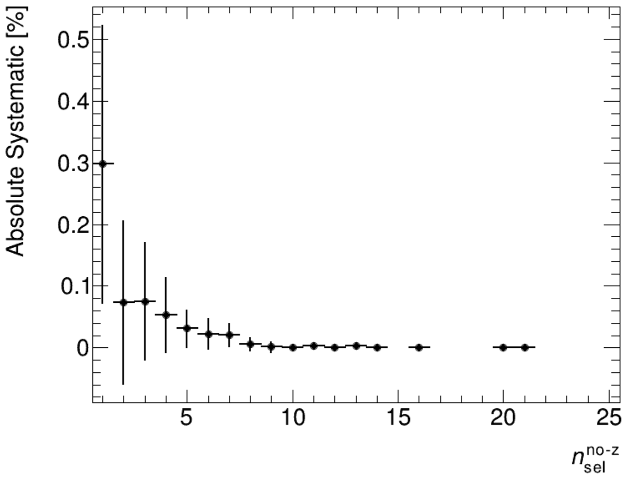

Figure 21: Systematic to the trigger efficiency due to non-uniform response. Calculated with Eq. (7) using data from Fig. 20.

5.3.3 Total Systematic Uncertainty

The only non-negligeable systematic uncertainties on the trigger efficiency are the selection uncertainty and the uncertainty from non-uniform response. Other sources of systematic uncertainty, such as the possibility that both signal and control trigger miss an important event, have been found to be negligible in previous Run 2 analyses [26]. The total uncertainty of the trigger efficiency is therefore obtained by adding the two non-neglibeable uncertainties in quadrature.

6 Beam Background

The beam pipe of the LHC is evacuated. However, this vacuum is not perfect. Therefore, sometimes a proton will interact with one of the residual gas molecules. If this happens near the ATLAS detector, the particles created in this interaction might enter the detector. There, they can cause the MBTS to fire, resulting in a contamination of the selected events. Events which are stored due to this process are called beam background events. The rate of beam background events among selected events R_{bgd} is investigate with two different methods: The Unpaired Events Method and the Fit Method.

Both methods use the time difference Δt between the MBTS A-side firing and the C-side firing to distinguish collision events and beam background events. If an event is from a collision at the interaction point, the particles will reach both disks of the MBTS at approximately the same time and the time difference will be close to zero. However, if an event is due to a beam background interaction outside of the detector, the particles will travel through the detector and reach the disks one after the other. The time difference for a particle at light velocity is then estimated to be $2 \cdot 3560\,\mathrm{mm}/c = 23.7\,\mathrm{ns}$.

Δt is calculated by subtracting the mean time of the C-side from the mean time of the A-side. Here mean time refers to the mean time of all modules on the respective side with time information and a charge deposition of at least 0.18 pC. All times are calibrated as described in Section 4.2.2. The threshold of 0.18 pC is chosen much higher than the threshold for the signal trigger (which is of the order of 0.01 pC) to remove any possible trigger bias.

In this section, R_{bgd} is calculated first using the Unpaired Events Method and then using the Fit Method. Afterwards the two methods and their results are compared and one method is chosen for the MinBias analysis.

6.1 Unpaired Events Method

The Unpaired Events Method estimates R_{bgd} by studying events from the unpaired trigger (definition in Section 2.3). This trigger selects events from unpaired bunch crossings where at least one MBTS module fired. This means that the signal trigger would have fired if the event was from a paired bunch crossing. In unpaired events there is no other bunch crossing to collide with and the data is being taken in a low pile-up enviroment. Therefore, it is assumed that these events are mostly from beam background and to a lesser degree from noise.

To verify this assumption, the time difference Δt is compared for signal events and unpaired events in Fig. 22a. If the mean time is not available on the A-side because none of the A-side modules above the energy threshold have time information, the event is artificially sorted into the bin at 74 ns. If it is not available for the C-side, the event is sorted into the bin at -74 ns. If it is not available for both sides, the event is sorted into the bin at 0 ns. Both for unpaired events as well as for signal events multiple peaks can be seen. Their position and width are retrieved by a gaussian fit. They are listed in Table 2. The uncertainties are estimated by varying the fit interval. The unpaired events have two side peaks but no main peak at $\Delta t = 0$. Their positions are at (-22.6 ± 0.2) ns and (21.9 ± 0.2) ns. This agrees well with the 23.7 ns expected for beam background events. Therefore, it can be assumed that the unpaired events with time information on both sides are mostly background events. Most of the signal events as expected peak approximately at 0. However, there are two side maxima at (-22.1 ± 0.2) ns and (22.1 ± 0.2) ns. This indicates that the signal events indeed are contaminated by beam background.

Unfortunately, the beam background can not be filtered out with the time information because only 66.7 % of events have time information available at both sides (see Section 4.2.1). However, the beam background events can be filtered out by applying certain cuts as can be seen in Figs. 22b to 22d. If a primary vertex is

Peak	Signal Events		Unpaired Events	
	μ[ns]	σ[ns]	μ[ns]	σ[ns]
Side Peak 1	-22.1 ± 0.2	3.3 ± 0.3	-22.6 ± 0.2	2.9 ± 0.3
Main Peak	-0.03 ± 0.05	1.9 ± 0.3	–	–
Side Peak 2	22.1 ± 0.2	3.2 ± 0.3	21.9 ± 0.2	2.8 ± 0.3

Table 2: Peak position μ and width σ of main and side peaks for signal events and unpaired events. They are obtained with a gaussian fit. The uncertainties are estimated by varying the fit interval. For the fit of the signal events the events with no time information on either side were not included in the 0 bin.

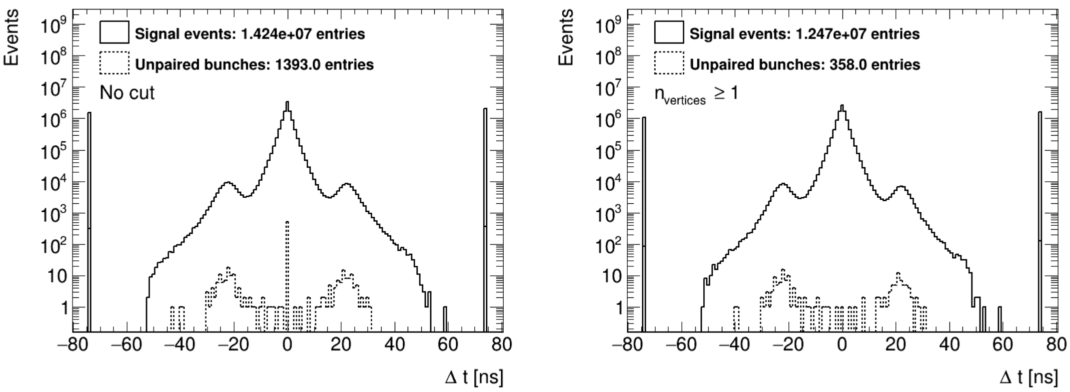

(a) Without Cuts

(b) Vertex Cut

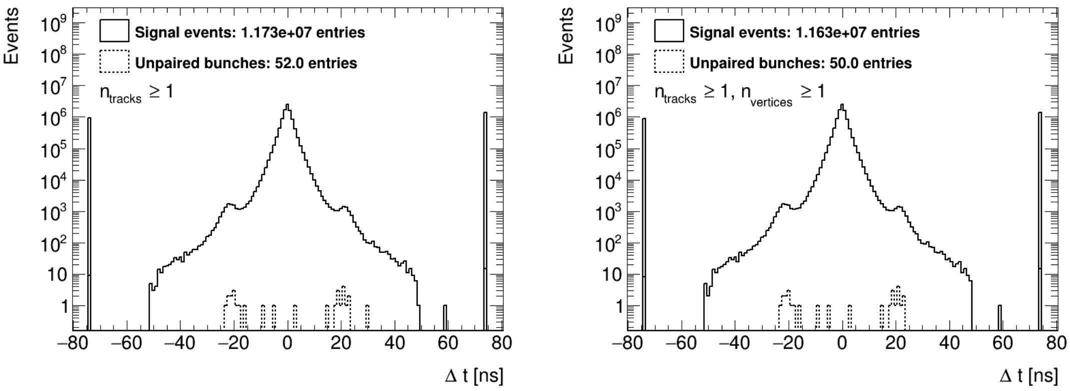

(c) Track Cut

(d) Vertex and Track Cut

Figure 22: Time difference Δt between A- and C-side for signal events (solid line) and events selected by the unpaired trigger (dashed). The time difference is calculated as described in Section 6 with corrected mean times as described in Section 4.2.2. If the mean time is unavailable on the A-side because none of the A-side modules above the energy threshold have time information, the event is artificially sorted into the bin at 74 ns. If it is unavailable for the C-side, the event is sorted into the bin at −74 ns. If it is unavailable for both sides, the event is sorted into the bin at 0 ns.

required, the number of events from unpaired bunches reduces from 1393 to 358 (compare Fig. 22b). This is a reduction of 74.3 %. The events that are rejected by the cut are mostly events where no time information is available on either side. This indicates that many of these events may actually be empty events that triggered the MBTS due to noise. Even more effective than the vertex cut is a cut on the number of tracks. If at least one selected track is required, the number of events from unpaired bunches drops by 96.3 % from 1393 to only 52 events (compare Fig. 22c). This cut also reduces the unpaired events with time information on both sides. If both cuts are combined, two more events are filtered out and the number of remaining events is 50 (compare Fig. 22d).

The rate of the beam background R_{bgd} is estimated to be the total number of events selected by the unpaired trigger divided by the total number of events selected by the signal trigger. However, the unpaired events must be scaled up beforehand to account for the following effects:

- The unpaired trigger runs on a prescale of 100 while the signal trigger is unprescaled.
- The ratio of paired and unpaired bunch crossings in the run is 64/16. This yields a scale factor of 4.
- During unpaired bunch crossings only one beam is present but during paired bunch crossings two beams are present. This makes beam background twice as likely for paired events.

Accordingly, the total scale factor is $100 \cdot 4 \cdot 2 = 800$. The rate of beam background therefore is $(7.8 \pm 0.2)\,\%$ before the cuts and $(0.34 \pm 0.05)\,\%$ after the cuts. The uncertainties on the rate are derived from the statistical uncertainty of the number of unpaired events, given by the square root of the number of unpaired events.

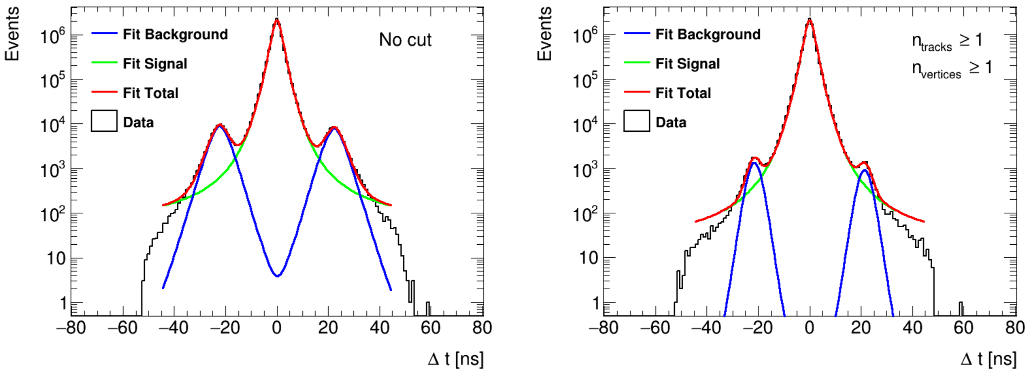

(a) Without Cuts

(b) Track and Vertex Cut

Figure 23: Fit of the time difference in the range [−45 ns, 45 ns]. $F(\Delta t)$ is shown in red. Its components f_{signal} and $f_{\text{bgd}} = f_{\text{bgd}+} + f_{\text{bgd}-}$ are shown in green and blue, respectively.

6.2 Fit Method

An alternative method to estimate the beam background is the Fit Method. In this method, the time differences for signal events are fitted with the function $F(\Delta t)$, which is composed of three sub-functions f_{signal}, $f_{\text{bgd}+}$, and $f_{\text{bgd}-}$, which describe the signal peak and the two side maxima from the beam background, respectively. The beam background rate can then be determined by integrating both the whole function and only the background components $f_{\text{bgd}+}$ and $f_{\text{bgd}-}$. All three sub-functions $f_i(\Delta t,\ a, b, c, \mu, \sigma, k)$ use the same equation but different parameters.

$$F(\Delta t) = f_{\text{signal}}(\Delta t) + f_{\text{bgd}+}(\Delta t) + f_{\text{bgd}-}(\Delta t) \tag{8}$$

$$f_i(\Delta t,\ a, b, \mu, \sigma, k) = a \cdot \exp\left(\frac{b}{1 + \sigma \cdot |\Delta t - \mu|^k}\right) \tag{9}$$

The parameters used in the fit are described in Table 3. The background peak functions share all their parameters except the parameters for the peak center and the peak height. The function $f_i(\Delta t,\ a, b, c, \mu, \sigma, k)$ used to model these peaks is not motivated by theory, but is heuristically chosen to visually match the data.

Parameters			Meaning
f_{signal}	$f_{\text{bgd}+}$	$f_{\text{bgd}-}$	
a_{signal}	$a_{\text{bgd}+}$	$a_{\text{bgd}-}$	peak height
0	$\mu_{\text{bgd}+}$	$\mu_{\text{bgd}-}$	peak center
σ_{signal}	σ_{bgd}		peak width
b_{signal}	b_{bgd}		sharpness of the peak
k_{signal}	k_{bgd}		steepness of the fall

Table 3: The parameters used for the fits of the time difference plots. $f_{\text{bgd}+}$ and $f_{\text{bgd}-}$ share the parameters σ_{bgd}, b_{bgd} and k_{bgd}. The parameter μ for f_{signal} is fixed at 0.

Figs. 23a and 23b show the fit of $F(x)$ to the time difference without any cuts and with both track and vertex cut applied. Also the components f_{signal} and $f_{\text{bgd}} = f_{\text{bgd}+} + f_{\text{bgd}-}$ are highlighted. The fit is performed in the interval [−45 ns, 45 ns] using only events where time information is available on both sides. The χ^2-values of the fits divided by their degrees of freedom are 245 (no cuts) and 290 (with cuts). The beam background rate is calculated by integrating the fit functions in the interval [−45 ns, 45 ns].

$$R_{\text{bgd}} = \frac{\int f_{\text{bgd}+}(\Delta t) + \int f_{\text{bgd}-}(\Delta t)}{\int F(\Delta t)} \tag{10}$$

The beam background rate is $(1.40 \pm 0.09)\,\%$ without cuts and $(0.136 \pm 0.006)\,\%$ with cuts. Its uncertainty is obtained by varying the fit limits and taking the standard deviation of R_{bgd}.

6.3 Comparison of the two Methods

Both methods yield a similar order of magnitude for the beam background rate: The Unpaired Events Method measures $(7.8 \pm 0.2)\,\%$ without cuts and $(0.34 \pm 0.05)\,\%$ with cuts. With the Fit Method one obtains $(1.40 \pm 0.09)\,\%$ without cuts and $(0.136 \pm 0.006)\,\%$ with cuts.
In previous analyses at lower center-of-mass energies, only the Unpaired Events Method was used [11, 27]. For the MinBias analysis at 13.6 TeV, the method has not yet been decided. The Unpaired Events Method is well tested and it yields conservative results. The Fit Method, however, needs further validation before it can be used in an analysis. It requires the choice of a fit function which is not based on theory and the resulting fits have χ^2/NDF-values above 200. Also, the Fit Method measures R_{bgd} only for events with time information on both sides. Therefore, it should be tested how much the choice of the fit function affects the measured beam background rate and whether R_{bgd} differs for events where time information is not available for both sides. Until these validations are completed, only the Unpaired Events Method is used to estimate the beam background.

7 Track Reconstruction Efficiency

For the measurement of the primary charged-particles multiplicity it is important that every charged particle is counted. However, the track reconstruction algorithm is not fully efficient. Therefore, the track reconstruction efficiency ($\varepsilon_{\mathrm{trk}}$) is measured in MC simulations and each track is weighted with the inverse of the tracking efficiency. $\varepsilon_{\mathrm{trk}}$ is defined as the fraction of primary charged particles in the simulation which have properly reconstructed tracks. It is measured as a function of η and p_T from the MC truth, i.e. the η and p_T of the generated particles real trajectory. The event selection and track selection are the same as for the regular MinBias analysis (see Section 3.1). A particle is considered properly reconstructed if a track with a matching probability $P_{\mathrm{match}} > 0.5$ exists. The matching probability P_{match} for a track and a particle is defined as the weighted fraction of clusters that are associated to both the track and the particle out of all the clusters associated to the track. A cluster is counted as associated with the particle if, according to the detector simulation software, the particle deposited more energy in that cluster than any other particle. The clusters are weighted depending on their importance in the reconstruction algorithm. The weight for clusters is 10 for all clusters in the Pixel Detector, 5 for all clusters of the SCT and 1 for all clusters in the TRT. The formula for P_{match} therefore is:

$$P_{\text{match}} = \frac{10 \cdot N_{\text{Pixel}}^{\text{common}} + 5 \cdot N_{\text{SCT}}^{\text{common}} + 1 \cdot N_{\text{TRT}}^{\text{common}}}{10 \cdot N_{\text{Pixel}}^{\text{track}} + 5 \cdot N_{\text{SCT}}^{\text{track}} + 1 \cdot N_{\text{TRT}}^{\text{track}}} \tag{11}$$

The resulting tracking efficiency, shown in Fig. 24a, assumes values between $(49.27 \pm 0.02)\,\%$ and $(86.96 \pm 0.09)\,\%$. The highest values are measured at high p_T and central η. The η-distribution of the tracking efficiency is shown in Fig. 24d for three exemplary p_T-slices. For each p_T-slice the tracking efficiency plateaus for $|\eta| < 0.7$. The value that the tracking efficiency assumes on the plateau is between $80\,\%$ in the lowest p_T-slice and $87\,\%$ in the highest one. For higher values of $|\eta|$ the tracking efficiency decreases with approximately constant slope. The p_T-distribution of the tracking efficiency is shown in Fig. 24c for three exemplary η-slices. For each η-slice the tracking efficiency quickly rises with p_T. The increase then slows down for the higher values of p_T.

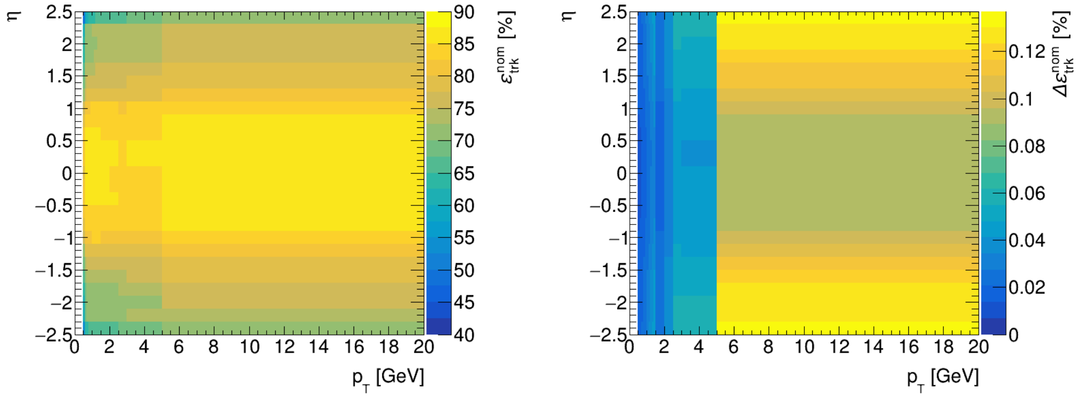

(a) Efficiency (b) Statistical Uncertainty

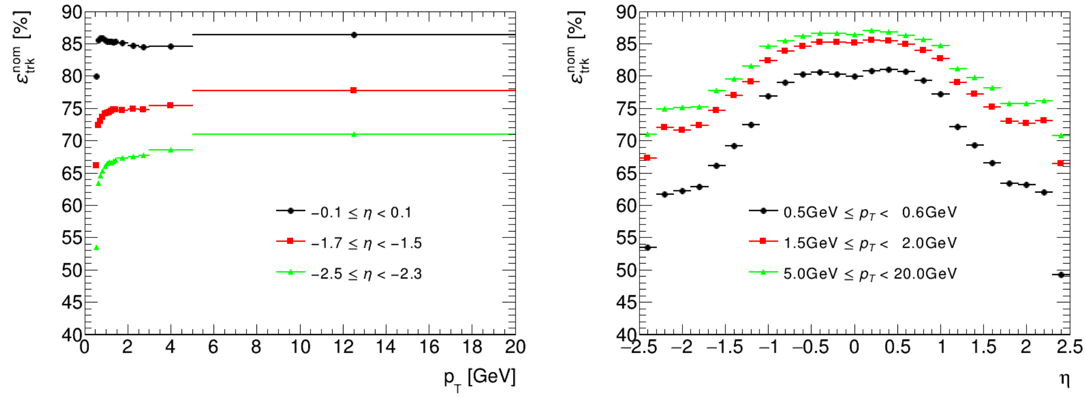

(c) p_T-dependency (d) η-dependency

Figure 24: Nominal track reconstruction efficiency. Data provided by the MinBias analysis group.

The statistical uncertainty of the tracking efficiency (see Fig. 24b) is consistently below 0.14 %. It is approximately constant in the plateau region and then increases with $|\eta|$. The uncertainty is especially high in the highest p_T slice where statistics are limited.

7.1 Material Estimation using the Extension Efficiency

The calculation of the track reconstruction efficiency relies on an accurate simulation of the ATLAS detector. In particular, the material distribution in the detector has to be well modeled. The PP0 region located between Pixel Detector and SCT (see Section 2.1.2) is known to be hard to model, but its material content can be deduced using the extension efficiency method. The first step in this method is the calculation of the extension efficiency. It is a measure of the number of tracks lost between the Pixel Detector and the SCT. The more material in this region, the higher the probability of a particle getting destroyed or severely deflected, resulting in a lower extension efficiency. The extension efficiency is compared between data and two MC simulations, the nominal simulation and the simulation with 25 % increased material density in the PP0 region. Then, the amount of material is extrapolated for which the MC simulation would match the extension efficiency measured in data.

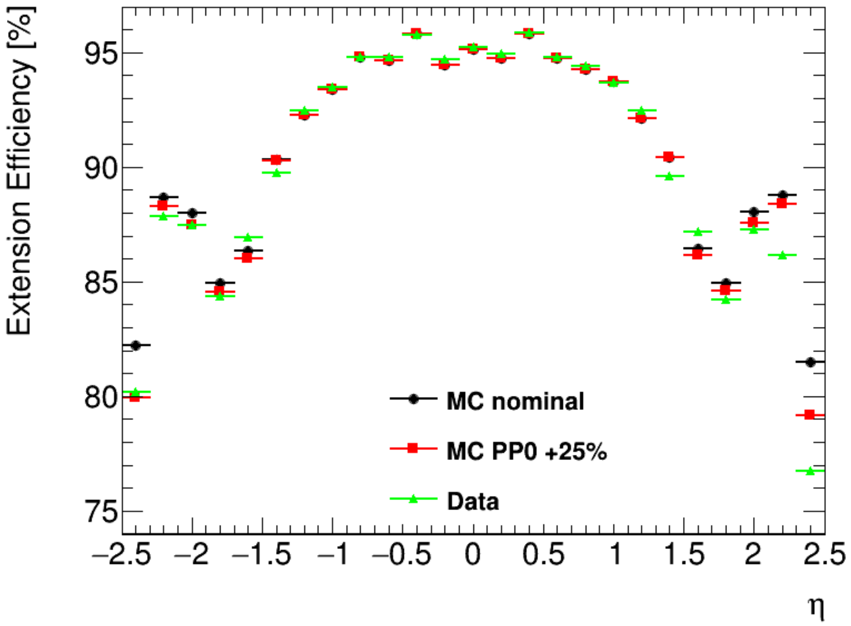

Figure 25: Extension Efficiency as a function of η for data (green) as well as the nominal (black) and the PP0 (red) sample.

7.1.1 Extension Efficiency

To measure the extension efficiency one looks at tracks that are reconstructed using only the Pixel Detector. They are called tracklets. If a tracklet can be extended to a full ID track, it is called a matched tracklet. Concretely, a tracklet is considered matched if it shares at least one hit with a full ID track. The extension efficiency (ε_{ext}) is the fraction of matched tracklets among all tracklets i.e. the fraction of Pixel Detector tracklets that can be continued to a full ID track. It is calculated as a function of the tracklets η.

$$\varepsilon_{\text{ext}}(\eta) = \frac{N_{\text{matched tracklets}}(\eta)}{N_{\text{all tracklets}}(\eta)} \tag{12}$$

Here, $N_{\text{all tracklets}}$ is the number of tracklets that meet the following selection criteria:

- $p_T < 500\,\text{MeV}$
- $|\eta| < 2.5$
- $|z_{\text{vtx}}| < 10\,\text{mm}$, where z_{vtx} is the primary vertexes z-position
- the tracklet has at least 4 pixel hits
- $|d_0| < 2\,\text{mm}$
- $|z_0 \sin\theta| < 2\,\text{mm}$

The d_0- and z_0-cuts are slightly loosened compared to the main analysis because the vertexing is less precise when only the Pixel Detector is used. The restriction on the primary vertexes position ensures that the origin area of the particles is small enough to be considered point-like. This is important because otherwise particles with the same η and ϕ will nonetheless travel through different detector regions due to the offsets of their primary vertices.

$N_{\text{matched tracklets}}$ is the number of tracklets that satisfy the selection criteria above and also share a hit with a full ID track which satisfies the following criteria:

- $p_T > 100\,\text{MeV}$
- At least four hits in the SCT

The p_T cut hardly removes any tracks and is mainly used for consistency with older analyses. The requirement on the number of hits in the SCT ensures that the particle indeed was lost between the Pixel Detector and the SCT and not further outside. For the calculation of the extension efficiency, all events with a primary vertex are used.

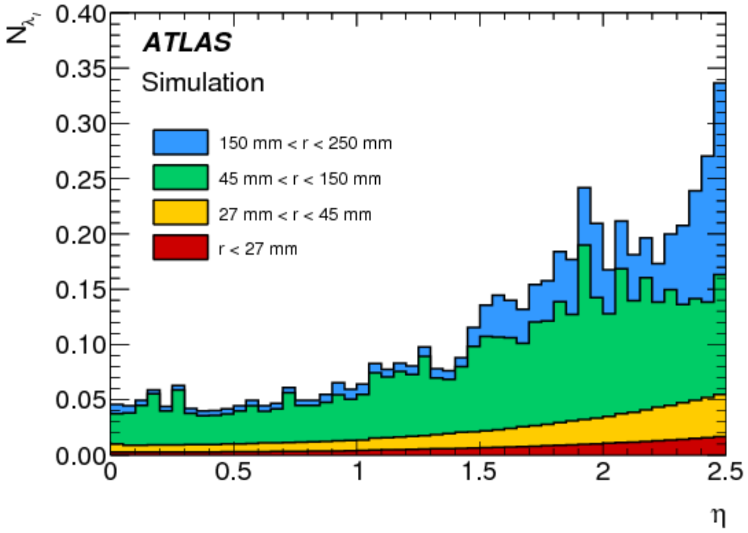

Figure 26: The amount of material associated with nuclear interactions, $N_{\lambda_I} = \int \mathrm{d}s\ \lambda_I^{-1}$, averaged over ϕ, as a function of η in the positive η range integrated up to $r = 250\,\mathrm{mm}$. The material within the Inner Detector is shown separately for the regions $r < 27\,\mathrm{mm}$, $27\,\mathrm{mm} < r < 45\,\mathrm{mm}$, $45\,\mathrm{mm} < r < 150\,\mathrm{mm}$ and $150\,\mathrm{mm} < r < 250\,\mathrm{mm}$, corresponding approximately to the beam pipe, IBL, pixel barrel and pixel service region, respectively. The statistical uncertainty in each bin is negligible. Taken from [15].

The extension efficiency measured in nominal and PP0 sample as well as in the data is depicted in Fig. 25. For the nominal sample it is approximately constant at around 95 % in the range $|\eta| < 0.9$ and then decreases until $|\eta| = 1.8$ where the extension efficiency is 84 %. It then recovers until it reaches a local maximum of about 87 % at $\eta = \pm 2.2$. In the outermost bins it drops to 82 %. This general behaviour is consistent with the material distribution measured during Run 2 shown in Fig. 26. The PP0 sample as expected matches the nominal sample in the central region ($|\eta| < 1.5$) and is lower in the PP0 region. The extension efficiency in the data, however, matches the MC prediction only up to $|\eta| \leq 1.3$ indicating that the discrepancies in the material description start already at the edges of the central region. At $|\eta| > 1.3$ the extension efficiency in data is consistently below the PP0 sample except for the bin at $1.5 < |\eta| < 1.7$ where it is even above the value of the nominal sample. Surprisingly, the extension efficiency measured in data is not symmetrical in η. The values on the A-side are lower than on the C-side, especially at high $|\eta|$. For example at $2.3 < |\eta| < 2.5$, the extension efficiency in data is 3.5 % lower on the A-side than on the C-side. About 20% of the effect can be attributed to an issue where turned-off pixel modules where described differently in the reconstruction of data and MC generated events. The other 80% are still the subject of ongoing studies. They might be an unintended side-effect of some changes to the track reconstruction algorithm that were applied between Run 2 and 3 in order to improve the algorithms speed.

7.1.2 Material Estimation

If a tracklet can not be matched to a track, this is usually because of interactions with the material between pixel and SCT. This can be a hadronic interaction where the particle is lost, or a scattering process that deflects the particle so much that the track reconstruction algorithm is unable to find the continuation of the tracklet. Therefore, the extension efficiency is expected to decrease as the material in the PP0 region increases. Run 2 studies based on MC simulations have shown that the decrease in the extension efficiency is linear to the amount of extra material [12]. Therefore, a MC simulation was produced where the material density in the PP0 region is increased by 25%. From the difference of the extension efficiency between the nominal MC sample and the PP0 sample the sensitivity a of the extension efficiency to material increases can be calculated:

$$a(\eta) = \frac{\varepsilon_{\text{ext}}^{\text{nom}}(\eta) - \varepsilon_{\text{ext}}^{\text{PP0}}(\eta)}{25\%} \tag{13}$$

The extension efficiency measured in data is then used to determine the percentage that the material in the PP0 region must be upscaled in order to measure the same ε_{ext} in MC simulations and data. Due to the linear relation between ε_{ext} and the extra material f_ρ one obtains the following formula for f_ρ.

$$f_\rho(\eta) = \frac{\varepsilon_{\text{ext}}^{\text{nom}}(\eta) - \varepsilon_{\text{ext}}^{\text{data}}(\eta)}{a(\eta)} = \frac{\varepsilon_{\text{ext}}^{\text{nom}}(\eta) - \varepsilon_{\text{ext}}^{\text{data}}(\eta)}{\varepsilon_{\text{ext}}^{\text{nom}}(\eta) - \varepsilon_{\text{ext}}^{\text{PP0}}(\eta)} \cdot 25\% \tag{14}$$

To check whether the material estimation from Run 2 is also applicable for Run 3, the extension efficiency of the nominal sample and the data is compared to the results from Run 2. Fig. 27 displays the extension efficiencies of Run 2 and Run 3 as well as their ratio for both MC and data. In general the MC simulations for Run 2 and 3 agree well with each other with a maximum discrepancy of less than 0.5 %. The only exception is the bins with $|\eta| > 2.0$ where the extension efficiency for Run 3 MC falls below the prediction from Run 2. This effect is stronger on the A-side than on the C-side: On the A-side, this discrepancy is up to 2.5 % ratio-wise, while the discrepancy on the C-side is only up to about 1.1 %. The extension efficiency in data also agrees within 0.5 % for $|\eta| < 1.9$. For higher $|\eta|$ the discrepancy grows up to 6.1 % on the A-side and 0.7 % on the C-side. Considering that the differences between MC simulation and data, which are used to calculate the material distribution, are of the same order of magnitude (maximum 3 % for Run 2), it is not possible to reuse the material distribution from Run 2. It has to be recalculated for Run 3.

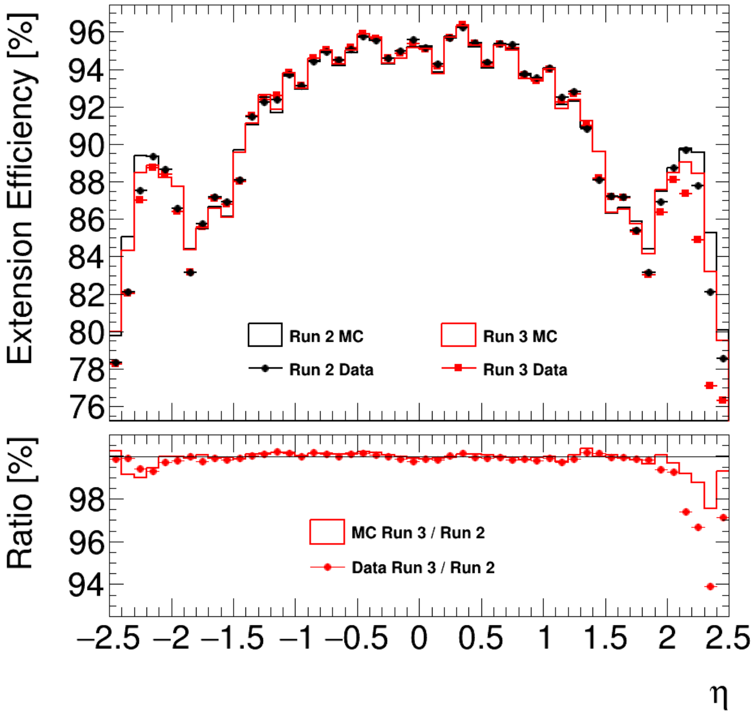

Figure 27: Comparison of the extension efficiency between Run 2 (black) and Run 3 (red). The lower pad shows the ratio of the extension efficiency in Run 3 divided by Run 2.

According to Eq. (14), the amount of extra material can be calculated by dividing the differences of the extension efficiency between the PP0 sample and the nominal sample as well as the data and the nominal sample. These differences are shown in Fig. 28. The difference between the two MC samples is approximately zero in the central region and 0.4 % in the PP0 region except in the outermost bins where it suddenly rises to 2.37 % (A-side) and 2.26 % (C-side). The differences between nominal MC and data are also close to zero in the central region except the outermost bins at $1.3 < |\eta| < 1.5$. They are in general higher than the differences between the MC samples with values roughly between 0.5% and 5% except for the two bins at $1.5 < |\eta| < 1.7$ where the extension efficiency for data is higher than for the MC sample. The asymmetry between A- and C-side is much stronger in data than in the MC simulation.
The resulting amounts of extra material can be seen in Fig. 29. It is only defined for $|\eta| > 1.5$ where the difference between the MC samples is non-negligible. The material discrepancy between data and MC in the bins $1.3 < |\eta| < 1.5$ can not be corrected. The extra material f_ρ is up to (172 ± 11) % on the A-side and (53 ± 12) % on the C-side. For the bins $1.5 < |\eta| < 1.7$, it is negative with (-57 ± 38) % (A-side) and (47 ± 42) % (C-side), meaning that the material distribution given to the MC overestimated the actual amount of material there. The reason for this is probably that some material was inserted closer to the interaction point than

planned, so some of the material that is expected in the $1.5 < |\eta| < 1.7$ bin is actually in the $1.3 < |\eta| < 1.5$ bin.

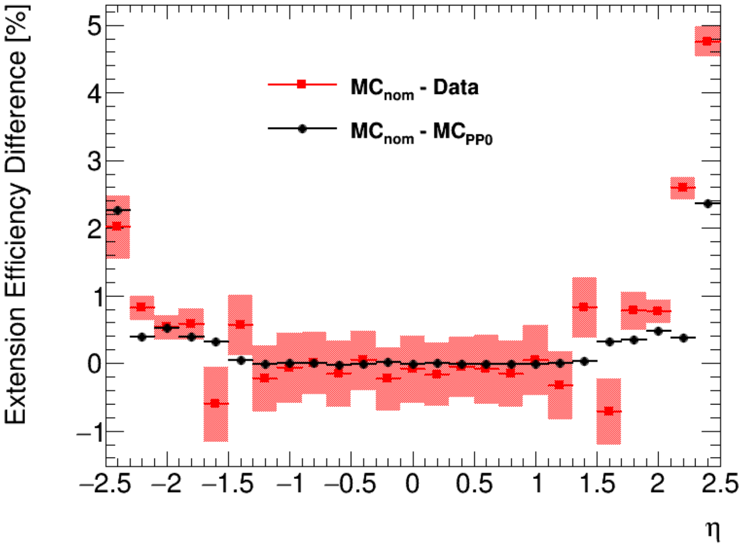

Figure 28: Difference of the extension efficiency. The statistical uncertainties are to small to be visible. The combined statistical and systematical uncertainties of the difference between nominal MC sample and data are indicated by the red boxes. For the difference between the two MC samples no systematic uncertainty is assumed.

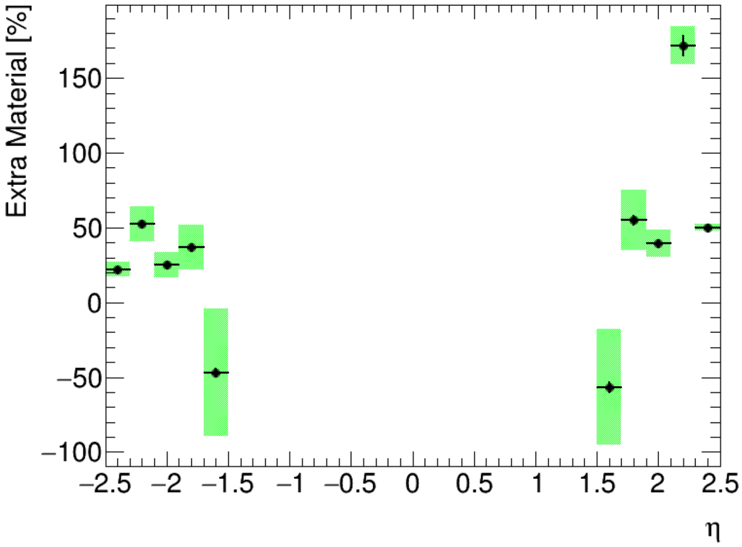

Figure 29: Extra Material in the PP0 region in percent of the material distribution used for the nominal MC sample. Combined systematical and statistical errors are indicated by the green boxes.

7.2 Correction to the Tracking Efficiency

To account for the updated material distribution, a correction to the track reconstruction efficiency is computed. The track reconstruction efficiency is expected to decrease as the material increases. In Run 2, the assumption that this decrease is linear in f_ρ agreed within statistical uncertainties with the results of four different MC simulations with extra material f_ρ ranging from 0% to 50% [26]. Therefore, the track reconstruction efficiency is corrected by a linear interpolation between the track reconstruction efficiency of the nominal sample $\varepsilon_{\text{trk}}^{\text{nom}}$ and the track reconstruction efficiency of the PP0 sample $\varepsilon_{\text{trk}}^{\text{PP0}}$ based on the extra material f_ρ.

$$\varepsilon_{\text{trk}}^{\text{corrected}}(\eta, p_T) = \varepsilon_{\text{trk}}^{\text{nom}}(\eta, p_T) - \frac{\varepsilon_{\text{trk}}^{\text{nom}}(\eta, p_T) - \varepsilon_{\text{trk}}^{\text{PP0}}(\eta, p_T)}{25\%} f_\rho(\eta) \tag{15}$$

If no extra material is measured, the track reconstruction efficiency will stay the same and if 25% extra material is measured, the corrected track reconstruction efficiency will assume the value of the PP0 sample $\varepsilon_{\text{trk}}^{\text{PP0}}$.

The correction to the tracking efficiency and its uncertainty are shown in Figs. 30a and 30b. It assumes values between $-0.9\,\%$ and $4.6\,\%$. The correction is highest for low p_T and high $|\eta|$.

The corrected tracking efficiency is shown in Fig. 31a. After the correction the tracking efficiency assumes values between $(44.9 \pm 0.2)\,\%$ and $(87.0 \pm 0.1)\,\%$. The biggest differences are in the high $|\eta|$ and low p_T region. This can be seen when comparing the p_T- and η-distributions shown in Figs. 31c and 31d with their counterparts for the uncorrected tracking efficiency Figs. 24c and 24d. Also the correction affects the A-side more than the C-side.

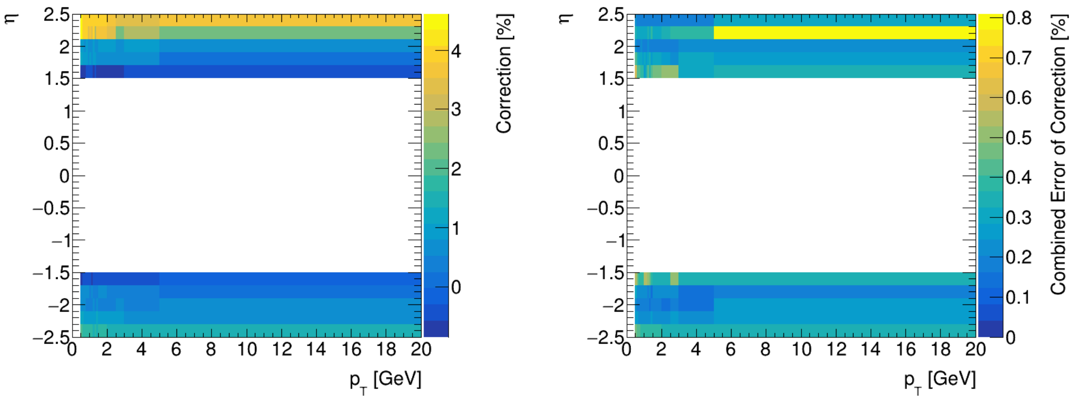

(a) Correction

(b) Uncertainty

Figure 30: Correction to the tracking efficiency due to the extra material in the PP0 region (left) and its combined statistical and systematic uncertainty (right).

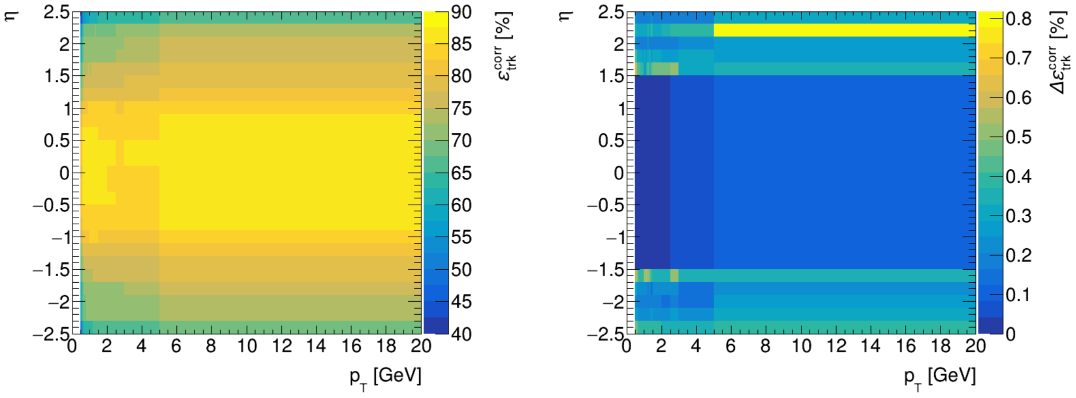

(a) Efficiency (b) Combined Uncertainty

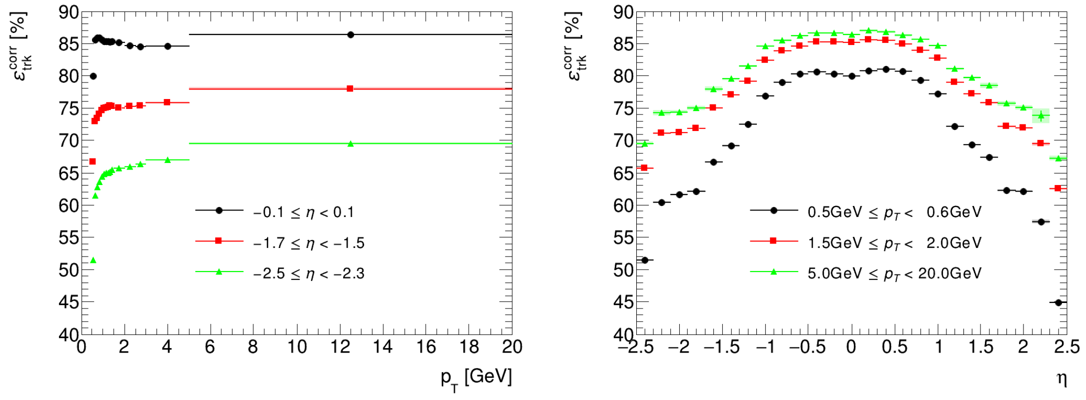

(c) p_T-dependency (d) η-dependency

Figure 31: Corrected track reconstruction efficiency. The boxes in (c) and (d) indicate the combined statistical and systematic uncertainties.

7.2.1 Systematic Uncertainties

Run 2 studies found two non-negligable sources of systematic uncertainties. They are uncertainties due to particle composition and due to fake tracklets [12].

Particle Composition The extension efficiency depends on the particle type (e.g. proton, kaon or electron) due to the fact that the particles have different interaction probabilities with matter. However, for the material estimation, only the general extension efficiency including all particle types is relevant. It is composed of the different extension efficiencies $\varepsilon_{\mathrm{ext}}^{t}$ for only one particle type t weighted by the fraction of tracklets of this type f_t.

$$\varepsilon_{\mathrm{ext}} = \sum_{t \in \mathrm{Types}} f_t \varepsilon_{\mathrm{ext}}^{t} \tag{16}$$

Unfortunately, different MC generators predict different rates of particles. For example, the predicted cross section of weakly-decaying strange baryons in EPOS is twice as big as the one of PYTHIA 8 [26]. It therefore can not be assumed

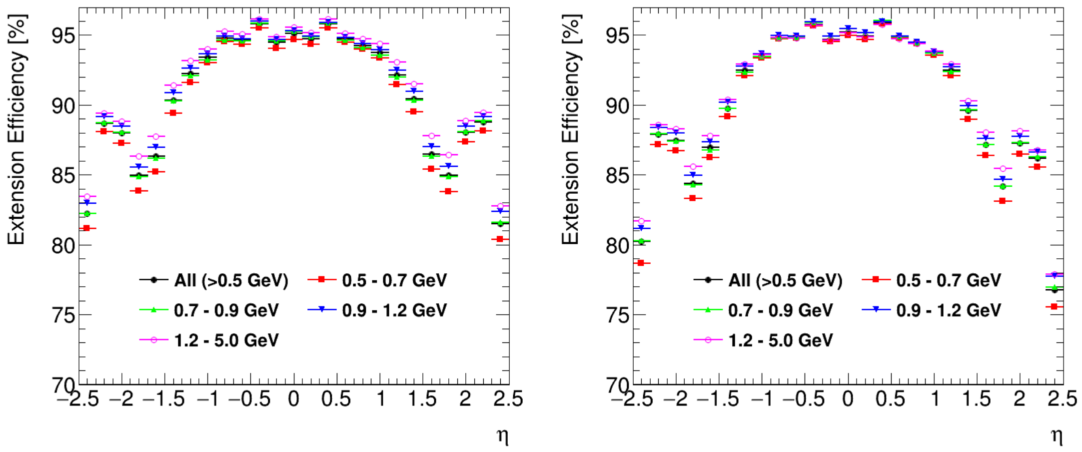

(a) MC Nominal (b) Data

Figure 32: Extension Efficiency in the different p_T regions for the MC nominal sample (left) and for data (right).

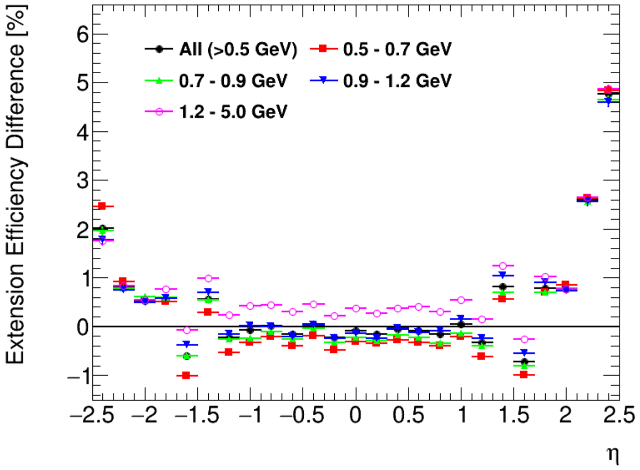

Figure 33: Extension efficiency difference between nominal sample and data $\Delta\varepsilon_{\text{ext}}$ in the different p_T regions.

that the particle composition f_t given by PYTHIA closely matches the particle composition in data. This results in a systematic uncertainty of the extension efficiency difference between MC and data.

To estimate this uncertainty, one uses that the p_T dependency of $\varepsilon^t_{\text{ext}}$ is different for each particle type and that the the particle composition f_t depends on p_T. Therefore, the extension efficiency is measured in four different p_T regions between 0.5 GeV and 5 GeV. This is shown in Fig. 32a for the nominal MC sample and Fig. 32b for data. The difference in the extension efficiency between MC and data $\Delta\varepsilon_{\text{ext}}$ is plotted in Fig. 33 for all p_T regions. The changes of $\Delta\varepsilon_{\text{ext}}$ between the regions reflect how slight variations of f_t and $\varepsilon^t_{\text{ext}}$ affect $\Delta\varepsilon_{\text{ext}}$. The values of $\Delta\varepsilon_{\text{ext}}$ in these four regions are compared with $\Delta\varepsilon_{\text{ext}}$ for the full p_T range ($p_T > 0.5\,\text{GeV}$).

The highest deviation is taken as a systematic uncertainty of the difference of the extension efficiency between the data and the nominal MC sample.

Fake Tracklets Due to combinatorial effects the track finding algorithm will usually reconstruct some tracklets that do not correspond to any real particle. These tracklets are called fake tracklets. The rate of fake tracklets is determined in MC simulations. In Run 2 the fake rate was below 0.3 % for all η bins [12]. To estimate the effect of fake tracklets on the extension efficiency, the fake tracklets in the MC are reweighted by ±50 % as is recommended in [28]. The resulting variation of the extension efficiency is then taken as a systematic uncertainty of the extension efficiency difference between data and MC. In Run 2, it was below 0.15 % across all η bins [12]. The recalculation of this systematic uncertainty would be out of the scope of this thesis. Therefore, the systematic uncertainty due to fake tracklets is assumed to be 0.15 % for all η bins. This is a conservative estimate especially in the central p_T region where the fake tracklet rate is small.

Total Systematic Uncertainty The total systematic uncertainty of the extension efficiency difference between data and MC is the quadratic sum of the uncertainties due to particle composition and fake tracklets. It is then propagated to the material estimation and to the correction of the tracking efficiency.

8 Summary and Outlook

The studies presented in this thesis provide essential inputs to the Minimum Bias analysis which measures distributions of primary charged-particles multiplicities in proton-proton collisions at 13.6 TeV.

The MinBias analysis relies on the MBTS as a trigger. Therefore, the module response of all MBTS modules is measured. Two MBTS modules are dead: one on the outer A-side and one on the inner C-side. Since the official time calibration for the MBTS has not yet been completed, a preliminary calibration of the MBTS times is performed.

The time difference between A- and C-side of the MBTS can be used to discriminate beam background from real signal events. Signal events have time differences close to zero, while beam background events are expected to have a time difference of ±23.7 ns. However, the time difference is only available for 66.7 % of all events. It can therefore not be used to filter out beam background. Instead, the beam background rate R_{bgd} is estimated using two different methods: the Unpaired Events Method and the Fit Method. The Unpaired Method assumes that events from unpaired bunch crossings are mostly from beam background. This assumption is supported by the time difference distribution for unpaired events which peaks near the expected value for beam background. To estimate R_{bgd}, the number of events from unpaired bunch crossings is scaled up to account for effects like trigger prescales and is then divided by the number of events from paired bunch crossings.

It is $(0.34 \pm 0.05)\,\%$ for the events that pass the event selection used in the MinBias analysis. The Fit Method estimates R_{bgd} by fitting the main peak and the side peaks of the time difference distribution for signal events (see Fig. 23). The beam background rate that follows out of this fit is $(0.136 \pm 0.006)\,\%$ for events passing the MinBias event selection. The Unpaired Events Method is well tested and it yields conservative results. The Fit Method, however, needs further validation before it can be used in an analysis. Until these validations are completed, only the Unpaired Events Method is used in the MinBias analysis to estimate the beam background.

For the unfolding of the primary charged-particles multiplicity distributions, each event is weighted with the inverse trigger efficiency. The trigger efficiency is the percentage of events selected by a randomly seeded control trigger that are also detected by the signal trigger. A plot of the trigger efficiency as a function of the selected tracks is given in Fig. 18. The trigger efficiency for events with only a single selected track is $(95.9 \pm 0.5)\,\%$. It increases with the number of tracks until it saturates at $100\,\%$ at 9 selected tracks. That is worse than the trigger efficiency measured in Run 2 which was $(98.9 \pm 0.5)\,\%$ for events with one selected track [11]. This can be attributed to the two dead MBTS modules.

The tracks for the η- and p_T-distributions are weighted by the inverse track reconstruction efficiency which is obtained from MC simulations. However, the material distribution used in these simulations is simplified in the PP0 region. Therefore, a correction to the tracking efficiency based on the Extension Efficiency Method is applied:

As a first step, the material distribution in the PP0 region is extrapolated by comparing the extension efficiency measured in data with the extension efficiency measured in two MC samples: the nominal sample which was used to calculate the tracking efficiency and a sample where the material density in the PP0 region was increased by $25\,\%$. The resulting material distribution shown in Fig. 29 is asymmetric between A- and C-side. This asymmetry is still the subject of ongoing investigations. Furthermore, the extension efficiency measured in data suggests that some material that was supposed to be inside the PP0 region has been inserted to close to the interaction point. This can not be corrected with the Extension Efficiency Method because the material density outside of the PP0 region was not scaled up in the simulation.

As a second step, the effect of the extra material on the tracking efficiency is calculated using the difference in the tracking efficiency of the two MC samples. The resulting correction can be seen in Fig. 30a. It takes values between $-0.9\,\%$ and $4.6\,\%$. The correction is largest in the high $|\eta|$ and low p_T region. The corrected track reconstruction efficiency is shown in Fig. 31.

The results in this thesis further our understanding of the MBTS and the triggers based on it, as well as the Inner Detector tracking. They will be used in the upcoming MinBias analysis to unfold the primary charged-particles multiplicity. All selected events will be weighted based on the trigger efficiency measured in this thesis. The MBTS performance studies explain why the trigger efficiency is lower than in Run 2 and will aid in the development of a time calibration for the MBTS. Furthermore, the fraction of beam background events among selected events is determined.

In addition to the events also all tracks in the MinBias analysis are weighted. Their weights are based on the track reconstruction efficiency. A data-driven correction to the track reconstruction efficiency is applied to account for the fact that the material description used for the MC simulation is simplified.

Using these results the MinBias analysis will soon be able to present primary charged-particles multiplicity measurements for $\sqrt{s} = 13.6\,\text{TeV}$, which will improve our understanding of the non-perturbative QCD region.

References

[1] The ATLAS Collaboration. *Charged-particle multiplicities in pp interactions measured with the ATLAS detector at the LHC*. New Journal of Physics 13 (2011), p. 053033. DOI: 10.1088/1367-2630/13/5/053033.

[2] The ATLAS Collaboration. *Charged-particle distributions in pp interactions at* $\sqrt{s} = 8$ *TeV measured with the ATLAS detector*. The European Physical Journal C 76 (2016). DOI: 10.1140/epjc/s10052-016-4203-9.

[3] The CMS cooperation. *Charged particle multiplicities in pp interactions at* $\sqrt{s} = 0.9$ *, 2.36, and 7 TeV*. Journal of High Energy Physics 2011 (2011). DOI: 10.1007/jhep01(2011)079.

[4] The CMS collaboration. *Transverse-Momentum and Pseudorapidity Distributions of Charged Hadrons in pp collisions at* $\sqrt{s} = 7$ *TeV*. Physical Review Letters 105 (2010). DOI: 10.1103/physrevlett.105.022002.

[5] The CMS collaboration. *Transverse-momentum and pseudorapidity distributions of charged hadrons in pp collisions at* $\sqrt{s} = 0.9$ *and 2.36 TeV*. Journal of High Energy Physics 2010 (2010). DOI: 10.1007/jhep02(2010)041.

[6] The ALICE collaboration. *Charged-particle multiplicity measurement in proton-proton collisions at* $\sqrt{s} = 7$ *TeV with ALICE at LHC*. The European Physical Journal C 68 (2010), pp. 345–354. DOI: 10.1140/epjc/s10052-010-1350-2.

[7] The CDF collaboration. *Measurement of Particle Production and Inclusive Differential Cross Sections in* $p\bar{p}$ *Collisions at* $\sqrt{s} = 1.96$*-TeV*. Phys. Rev. D 79 (2009), p. 112005. DOI: 10.1103/PhysRevD.79.112005. arXiv: 0904.1098 [hep-ex].

[8] The CMS collaboration. *Pseudorapidity distribution of charged hadrons in proton-proton collisions at* $\sqrt{s} = 13$ *TeV*. Phys. Lett. B 751 (2015), pp. 143–163. DOI: 10.1016/j.physletb.2015.10.004. arXiv: 1507.05915 [hep-ex].

[9] The UA1 collaboration. *A study of the general characteristics of proton-antiproton collisions at s=0.2 to 0.9 TeV*. Nuclear Physics B 335 (1990), pp. 261–287. ISSN: 0550-3213. DOI: 10.1016/0550-3213(90)90493-W. URL: https://www.sciencedirect.com/science/article/pii/055032139090493W.

[10] The UA5 collaboration. *Charged particle multiplicity distributions at 200 and 900 GeV c.m. energy*. Zeitschrift für Physik C Particles and Fields 43 (1989), pp. 357–374. DOI: 10.1007/BF01506531.

[11] The ATLAS Collaboration. *Charged-particle distributions in $\sqrt{s} = 13$ TeV pp interactions measured with the ATLAS detector at the LHC*. Phys. Lett. B 758 (2016), pp. 67–88. DOI: 10.1016/j.physletb.2016.04.050. arXiv: 1602.01633. URL: https://cds.cern.ch/record/2128621.

[12] Valentina Cairo. *Charged-Particle Distributions and Material Measurements in $\sqrt{s} = 13$ TeV pp collisions with the ATLAS Inner Detector*. 2017. URL: https://cds.cern.ch/record/2291081.

[13] The ATLAS Collaboration. *The ATLAS Experiment at the CERN Large Hadron Collider: A Description of the Detector Configuration for Run 3*. Tech. rep. CERN, 2023. arXiv: 2305.16623. URL: https://cds.cern.ch/record/2859916.

[14] The ATLAS Collaboration. *The ATLAS Experiment at the CERN Large Hadron Collider*. Journal of Instrumentation 3 (2008). DOI: 10.1088/1748-0221/3/08/S08003.

[15] The ATLAS Collaboration. *Study of the material of the ATLAS inner detector for Run 2 of the LHC*. JINST 12 (2017). DOI: 10.1088/1748-0221/12/12/P12009. arXiv: 1707.02826. URL: https://cds.cern.ch/record/2273894.

[16] The ATLAS Collaboration. *The Optimization of ATLAS Track Reconstruction in Dense Environments*. Tech. rep. CERN, 2015. URL: https://cds.cern.ch/record/2002609.

[17] Gaogalalwe Mokgatitswane et al. *The replacement of Crack and MBTS Scintillator Detector Modules for Phase-I Upgrade of the Tile Calorimeter*. Tech. rep. CERN, 2021. URL: https://cds.cern.ch/record/2758937.

[18] *ATLAS TWiki*. URL: https://twiki.cern.ch/twiki/bin/view/Atlas/SpecialModules. Accessed 07/15/23.

[19] G. Mokgatitswane, T. J. Lepota, and B. Mellado. “The replacement and refurbishment of Gap Scintillator Counters for the ATLAS Tile Calorimeter Phase I Upgrade”. *The Proceedings of SAIP2021, the 65th Annual Conference of the South African Institute of Physics*. Ed. by Aletta Prinsloo. 2021, pp. 132–137. ISBN: 978-0-620-97693-0. URL: https://events.saip.org.za/event/206/page/446-the-proceedings-of-saip2021.

[20] S. Porteboeuf, T. Pierog, and K. Werner. *Producing Hard Processes Regarding the Complete Event: The EPOS Event Generator*. 2010. arXiv: 1006.2967 [hep-ph].

[21] Torbjörn Sjöstrand, Stephen Mrenna, and Peter Skands. *A brief introduction to PYTHIA 8.1*. Computer Physics Communications 178 (2008), pp. 852–867. ISSN: 0010-4655. DOI: 10.1016/j.cpc.2008.01.036.

[22] The ATLAS Collaboration. *Further ATLAS tunes of PYTHIA6 and Pythia 8*. Tech. rep. CERN, 2011. URL: https://cds.cern.ch/record/1400677.

[23] P. Skands, S. Carrazza, and J. Rojo. *Tuning PYTHIA 8.1: the Monash 2013 tune*. The European Physical Journal C 74 (2014). DOI: 10.1140/epjc/s10052-014-3024-y.

[24] S. Ostapchenko. *Monte Carlo treatment of hadronic interactions in enhanced Pomeron scheme: QGSJET-II model*. Physical Review D 83 (2011). DOI: 10.1103/physrevd.83.014018.

[25] *ATLAS Run Query*. URL: https://atlas-runquery.cern.ch.

[26] Anthony Keith Morley et al. *Supporting note for the Minimum Bias publication: Charge particle multiplicity in pp interactions at 13 TeV measured with the ATLAS detector*. Tech. rep. CERN, 2015. URL: https://cds.cern.ch/record/2011604.

[27] F. Guescini, A. Lister, and S. Nektarijevic. *Beam Background Studies for the Minimum Bias Measurements from p-p Interactions at $\sqrt{s} = 900$ GeV*. Tech. rep. CERN, 2010. URL: https://cds.cern.ch/record/1235383.

[28] The ATLAS Collaboration. *Early Inner Detector Tracking Performance in the 2015 data at $\sqrt{s} = 13$ TeV*. Tech. rep. CERN, 2015. URL: https://cds.cern.ch/record/2110140.

Erklärung

Ich versichere, dass ich diese Arbeit selbstständig verfasst und keine anderen als die angegebenen Quellen und Hilfsmittel benutzt habe.

Heidelberg, den 17. Juli 2023,

Florian Frauen